Inorganic Chemistry
Article
Cite This: *Inorg. Chem.* 2019, 58, 12025−12039
pubs.acs.org/IC

Effect of Stacking Interactions on the Translation of Structurally Related Bis(thiosemicarbazonato)nickel(II) HER Catalysts to Modified Electrode Surfaces

Alexander J. Gupta,[†,§] Nicholas S. Vishnosky,[‡,§] Oleksandr Hietsoi,[‡] Yaroslav Losovyj,[⊥] Jacob Strain,[‡] Joshua Spurgeon,[∥] Mark S. Mashuta,[‡] Rahul Jain,[‡] Robert M. Buchanan,[‡] Gautam Gupta,[*,†] and Craig A. Grapperhaus[*,‡]

[†]Department of Chemical Engineering, [‡]Department of Chemistry, [∥]Conn Center for Renewable Energy Research, University of Louisville, Louisville, Kentucky 40292, United States

[⊥]Department of Chemistry, Indiana University—Bloomington, Bloomington, Indiana 47405, United States

Supporting Information

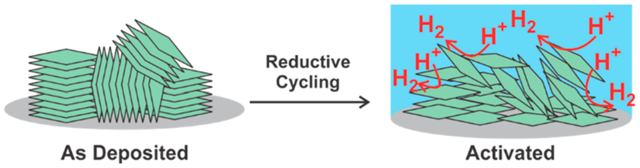

ABSTRACT: A series of crystalline nickel(II) complexes (**1**−**3**) based on inexpensive bis(thiosemicarbazone) ligands diacetylbis(4-methyl-3-thiosemicarbazone) (H_2ATSM), diacetylbis(4,4-dimethyl-3-thiosemicarbazone) (H_2ATSDM), and diacetylbis[4-(2,2,2-trifluoroethyl)-3-thiosemicarbazone] (H_2ATSM-F_6) were synthesized and characterized by single-crystal X-ray diffraction and NMR, UV−visible, and Fourier transform infrared spectroscopies. Modified electrodes **GC-1**−**GC-3** were prepared with films of **1**−**3** deposited on glassy carbon and evaluated as potential hydrogen evolution reaction (HER) catalysts. HER studies in 0.5 M aqueous H_2SO_4 (10 mA cm^{-2}) revealed dramatic shifts in the overpotential from 0.740 to 0.450 V after extended cycling for **1** and **2**. The charge-transfer resistances for **GC-1**−**GC-3** were determined to be 270, 160, and 630 Ω, respectively. Characterization of the modified surfaces for **GC-1** and **GC-2** by scanning electron microscopy and Raman spectroscopy revealed similar crystalline coatings before HER that changed to surface-modified crystallites after conditioning. The surface of **GC-3** had an initial glasslike appearance before HER that delaminated after HER. The differences in the surface morphology and the effect of conditioning are correlated with crystal-packing effects. Complexes **1** and **2** pack as columns of interacting complexes in the crystallographic *a* direction with short interplanar spacings between 3.37 and 3.54 Å. Complex **3** packs as columns of isolated molecules in the crystallographic *b* direction with long-range interplanar spacings of 9.40 Å.

■ INTRODUCTION

Increasing worldwide demand for cheap energy has fueled the need to develop sustainable alternative energy sources.[1] Hydrogen offers great potential as a carbon-free alternative to fossil fuels.[2] One of the major challenges in this area is the development of artificial water-splitting catalysts based on solid-state materials and molecular electrocatalysts that efficiently produce O_2 and H_2 from water utilizing either solar energy[3−6] or electrolysis.[7,8] Platinum is the "gold standard" catalyst for H_2 production via the hydrogen evolution reaction (HER) in aqueous acidic solutions. However, its practical widespread utility in electrocatalytic devices is limited by its scarcity and high cost.[9,10] This has stimulated the development of new electrocatalysts containing earth-abundant transition metals, such as iron,[11] cobalt,[12] nickel,[13] copper,[14] and molybdenum,[15−17] as metal phosphides,[12,18] selenides,[19] sulfides,[20,21] and small-molecule complexes.[22−28] Of these materials, molybdenum sulfides stand out as an economical alternative to platinum.[29−31] Their high activity is thought to arise from the location and number of *cis*-sulfur edge sites in their layered structures.[31] Moreover, Schaak and co-workers reported inexpensive and nonnoble nickel phosphide[32] and iron phosphide[33] nanoparticles that are highly effective for HER. Nickel−molybdenum nitride nanosheets have also demonstrated effectiveness in catalyzing HER.[34]

There is consensus that most homogeneous molecular electrocatalysts generate reactive metal hydride intermediates during HER.[25,35−38] Several of these electrocatalysts display low overpotential, high turnover frequencies, and faradaic efficiencies in excess of 90%.[38,39] Noncovalent modification of electrode surfaces with catalysts has been studied for various applications.[40−43] There is an emerging interest in the modification of electrode surfaces with small-molecule HER catalysts.[44−50] Most notably, Fontecave and co-workers developed multiwalled carbon nanotube $[Ni(P^{Ph}{}_2N^{Ph}{}_2)_2]$ modified electrodes that display high catalytic activity at low overpotential.[51] We reported the translation of activity and mechanism of a rhenium thiolate HER catalyst from solution to modified electrodes.[52] Other examples of heterogeneous molecular catalysts for HER include Co complexes of

Received: April 24, 2019
Published: September 3, 2019

DOI: 10.1021/acs.inorgchem.9b01209
Inorg. Chem. 2019, 58, 12025−12039

(dmgBF2)2 with carbon black on Nafion-coated glassy carbon[45] and cobaloxime-modified electrodes[45,46] as well as cobalt porphyrin,[47,48,53] metal phthalocyanine,[54−57] and an organometallic complex incorporated in a Nafion film.[58] However, these complexes either require high overpotentials and/or are unstable over prolonged electrolysis, reducing their practical use as HER catalysts.

The instability of surface-adsorbed electrocatalysts has been of concern since the observation that some cobalt[59−61] and nickel[62,63] complexes decompose to metal-containing nanoparticles during HER. Studies by Dempsey and co-workers[64,65] and Wombwell and Reisner[66] highlight the importance of ligand design in catalyst preparation. These studies evaluated the stability of imine- and thiolate-containing chelates during HER and showed that Ni−S and ligand C═N bonds may be susceptible to hydrogenation, leading to catalyst degradation and electrodeposition of metal-based nanoparticles.

Recently, we, and others, have explored the use of thiosemicarbazone ligands in the design of new HER electrocatalysts. The thiosemicarbazone ligands are redox-noninnocent and can function as a reservoir for charge with hydrogen evolution at either the metal or ligand. The HER mechanism proceeds via ligand-assisted metal-centered,[67] ligand-centered,[68−70] or metal-assisted ligand-centered reactivity depending on the identity of the metal.[28,69,71] Herein, we report the synthesis, characterization, and electrocatalytic behavior of a series of structurally related bis(thiosemicarbazonato)nickel(II) complexes (Scheme 1) deposited on glassy carbon electrode (GCE) surfaces. The ligands are obtained in high yields using readily available and inexpensive organic reagents according to literature methods.[72,73] The resulting nickel(II) complexes have been characterized by NMR, Fourier transform infrared (FT-IR), and UV−visible spectroscopies, X-ray crystallography, and cyclic voltammetry in acetonitrile prior to deposition on GCEs. Drop-casting acetonitrile inks of the nickel complexes on GCEs produce uniform coatings that were characterized by spectroscopy and microscopy methods before and after HER catalysis in aqueous acidic solutions.

Scheme 1. Synthesis and Labeling Scheme of Complexes 1−3

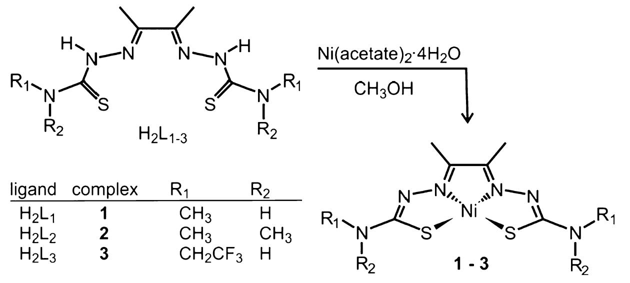

ligand	complex	R_1	R_2
H_2L_1	1	CH_3	H
H_2L_2	2	CH_3	CH_3
H_2L_3	3	CH_2CF_3	H

RESULTS AND DISCUSSION

Synthesis and Characterization. The ligands diacetylbis(4-methyl-3-thiosemicarbazone) (H_2ATSM),[72] diacetylbis(4,4-dimethyl-3-thiosemicarbazone) (H_2ATSDM),[73] and diacetylbis[4-(2,2,2-trifluoroethyl)-3-thiosemicarbazone] (H_2ATSM-F_6)[73] were prepared as previously reported. The nickel(II) complexes **1**−**3** were synthesized using the methodology established for the preparation of **1**[72] (Scheme 1). The newly reported **2** and **3** were characterized by elemental analysis, cyclic voltammetry, mass spectrometry, NMR, FT-IR, and UV−visible spectroscopies, and X-ray crystallography. The ^{1}H NMR spectra of **2** and **3** (Figures S1 and S2) are consistent with their proposed structures. The IR spectra (Figures S3 and S4) show shifts of ν_{C-N} stretches relative to the free ligand associated with nickel(II) coordination. All of the complexes are green in color upon dissolution in acetonitrile. The ligand-to-ligand charge-transfer transitions[72] in the UV−visible spectrum slightly increase in energy from **2** to **1** to **3** (Figure S5).

The solid-state structures of **2** and **3** were determined by single-crystal X-ray diffraction for comparison with the known structure of **1**.[74] Crystals of **2** and **3** were obtained as orange prisms and red-brown plates, respectively, via slow evaporation of an acetonitrile solution layered with ether. Crystallographic data and structure refinement details are listed in Table S1. The crystal lattices of **1** and **3** include an acetonitrile solvate molecule, while the lattice of **2** is not solvated.

The ORTEP[75] representations of **2** and **3** in Figure 1, top and bottom, respectively, show that each contains a square-planar nickel(II) in an N_2S_2 donor environment. Selected bond distances and angles for **1**−**3** are provided in Table S2. The Ni−N distances are statistically equivalent over the series with an average value of 1.856(5) Å. Further, there are no significant differences in the Ni−S bond distances, which have an average value of 2.1568(18) Å. The similarities in the metric parameters are also observed in the bond distances within the ligand framework. For all three nickel complexes, the bond distances are consistent with a conjugated π system of alternating single and double bonds.[76] Comprehensive lists of bond distances and angles can be found in Tables S3 and S4.

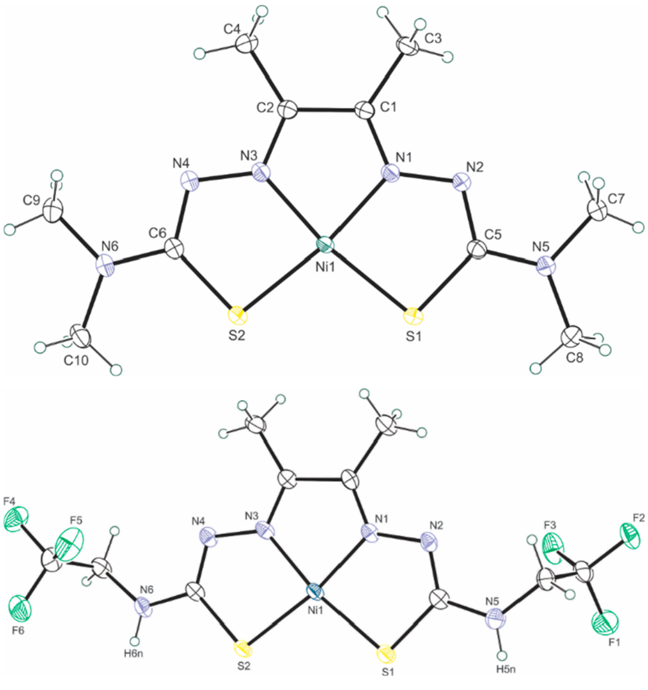

Figure 1. ORTEP[75] views (50% probability) of **2** (top) and **3** (bottom) showing atom labeling for non-hydrogen atoms in the asymmetric unit.

Overall, the structures of **1**−**3** are best described as square-planar. Both **1** and **2** are rigorously planar with all non-hydrogen atoms in or near the best-fit plane. For **1**, the best-fit plane of all 17 non-hydrogen atoms has a standard deviation of ±0.032 Å, with the largest deviation of ±0.067 Å for S2. Similarly, in **2**, the standard deviation from the best-fit plane of all 19 non-hydrogen atoms is ±0.053 Å, with the largest deviation of ±0.126 Å for C3. The pendant $-CH_2CF_3$ groups of **3** disrupt the overall planarity of that molecule. However, except for the $-CF_3$ moieties, the non-hydrogen atoms define a plane with a standard deviation of ±0.033 Å, with the largest deviation of ±0.083 Å for S2. The $-CF_3$ carbon atom C8 sits 1.46 Å above the best-fit plane for **3**, whereas C10 lies 1.43 Å below the plane.

The crystal-packing arrangements for the rigorously planar **1** and **2** display similar columns of paired complexes stacked along the *a* axes (Figure 2, top and middle, respectively). The bulkier $-CH_2CF_3$ groups in **3** preclude complex pairing, resulting in long-range stacking along the *b* axis (Figure 2, bottom). For **1**, the "inverse pair" of complexes containing Ni (*x*, *y*, *z*) and Ni′ (1 − *x*, 1 − *y*, 1 − *z*) stack with an interplanar distance of 3.48 Å. These inverse pairs form a column of complexes generated by translation along the *a* axis. The interplanar distance between Ni′ (*x*, *y*, *z*) and Ni″ (1 + *x*, *y*, *z*) is 3.47 Å. Neighboring columns, with equivalent spacings, are generated by the 2_1 screw axis (Ni‴) and *c* glide (Ni⁗) associated with the space group $P2_1/c$. Complex **2**, which crystallizes in the space group $P\bar{1}$, displays similar columns generated by translation of the inverse pair Ni (*x*, *y*, *z*) and Ni′ (1 − *x*, 1 − *y*, 1 − *z*) along the *a* axis with interplanar distances of 3.54 and 3.37 Å for Ni/Ni′ and Ni′/Ni″, respectively. The crystal packing of **3** is unique because the bulkier $-CH_2CF_3$ groups prevent stacking of inverse pairs. As shown in Figure 2, Ni (*x*, *y*, *z*) and Ni′ (1 − *x*, 1 − *y*, 1 − *z*) are contained in separate, neighboring columns directed along the *b* axis. In contrast to **1** and **2**, the interplanar distances for the columns of **3** are long, 9.40 Å, because each member of the column is generated by a translation in the *b* direction.

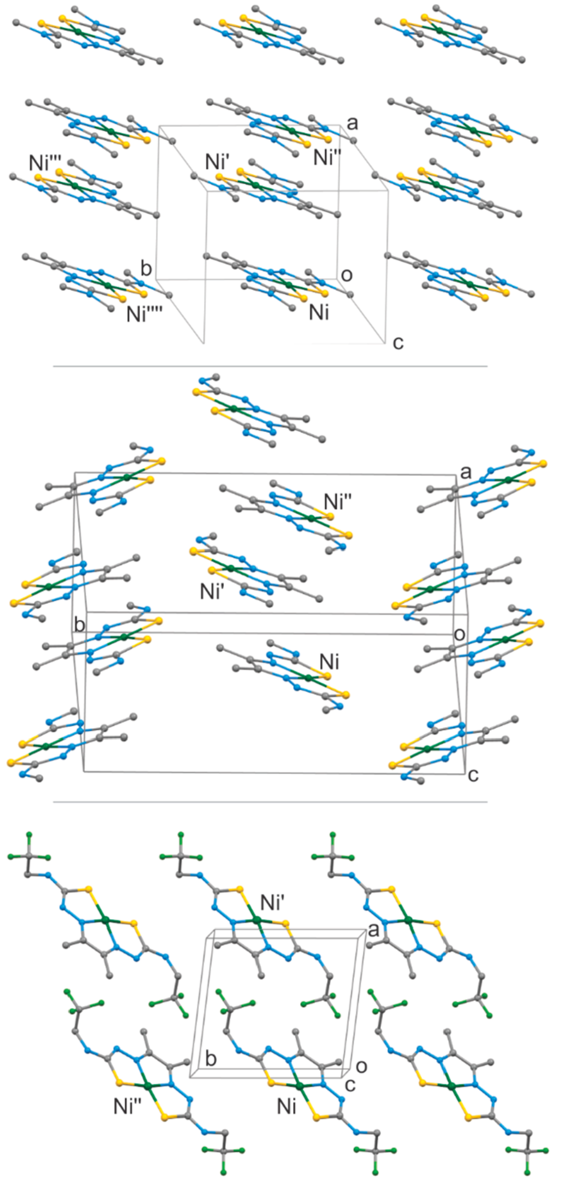

Figure 2. Packing diagrams for **1** (top), **2** (middle), and **3** (bottom). Individual labels are associated with the following symmetry operations: Ni, *E* (*x*, *y*, *z*); Ni′, *i* (1 − *x*, 1 − *y*, 1 − *z*), Ni″, translation along *a* (1 + *x*, *y*, *z*) for **1** and **2** or along *b* (*x*, 1 + *y*, *z*) for **3**; Ni‴, 2_1 (1 − *x*, 0.5 + *y*, 1.5 − *z*); Ni⁗, *c* glide (*x*, 1.5 − *y*, 0.5 + *z*).

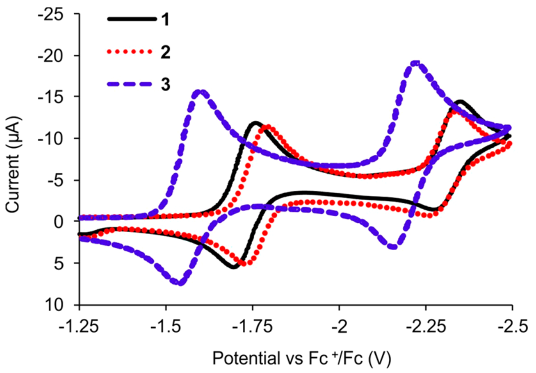

Figure 3. Cyclic voltammograms of **1** (black trace), **2** (red trace), and **3** (blue trace) in acetonitrile at 1 mM concentration with 0.1 M TBAHFP as the supporting electrolyte. Scan rate = 50 mV s^{-1}; potentials referenced versus Fc^+/Fc.

Table 1. Reduction Potentials versus Fc^+/Fc and Peak Separation for 1−3 in Acetonitrile Containing 0.1 M TBAHFP as the Supporting Electrolyte

	$E_{1/2}$, V (Δ*E*, mV)	
complex	L/L$^-$	nickel(II/I)
1	−1.73 (64)	−2.31 (78)
2	−1.76 (62)	−2.30 (73)
3	−1.57 (59)	−2.19 (64)

Homogeneous Electrochemical Characterization. Cyclic voltammograms of **1**−**3** (Figure 3) show two reversible events at potentials more cathodic than −1.3 V versus ferrocenium/ferrocene (Fc^+/Fc) in acetonitrile containing 0.1 M tetrabutylammonium hexafluorophosphate (TBAHFP) as the supporting electrolyte. The more anodic event is assigned to a ligand-centered reduction, and the more cathodic event is assigned to the nickel(II/I) redox couple (Table 1). The locations of these reductive events were previously established by density functional theory calculations by our laboratory[77] and others.[25] The ligand- and metal-centered $E_{1/2}$ values for **1** occur at −1.73 and −2.31 V versus Fc^+/Fc, respectively. The pendant secondary amines of **1** are replaced with tertiary amines in **2**, resulting in an ~30 mV cathodic shift in the

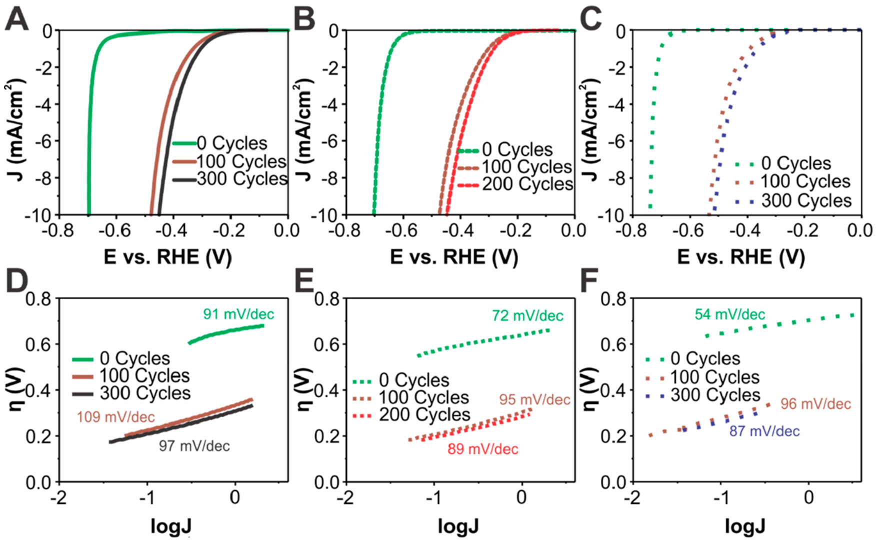

Figure 4. Effects of reductive cycling from 0 to −0.8 V vs RHE at 50 mV s^{-1} on the performance of the three modified electrodes. (A) polarization curves for **GC-1** which exhibits peak HER performance after 300 cycles. (B) polarization curves for **GC-2** which exhibits peak HER performance after 200 cycles. (C) polarization curves for **GC-3** which exhibits peak performance after 300 cycles. (D) Tafel slopes for **GC-1** before and after 300 cycles. (E) Tafel slopes for **GC-2** before and after 200 cycles. (F) Tafel slopes for **GC-3** before and after 300 cycles.

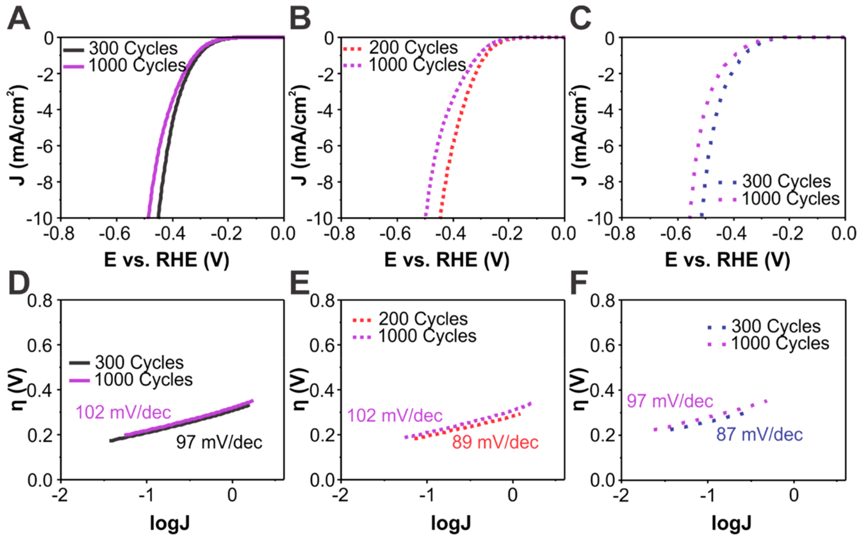

Figure 5. Effects of reductive cycling from 0 to −0.8 V vs RHE at 50 mV s^{-1} on the performance of the three modified electrodes past peak activity. (A) polarization curves for **GC-1**, revealing that its performance diminishes following 300 cycles. (B) polarization curves for **GC-2**, revealing that its performance diminishes following 200 cycles. (C) polarization curves for **GC-3**, revealing that its performance diminishes following 300 cycles. (D) Tafel slopes for **GC-1** at 300 and 1000 cycles. (E) Tafel slopes for **GC-2** at 200 and 1000 cycles. (F) Tafel slopes for **GC-3** at 300 and 1000 cycles.

ligand-centered reduction potential, −1.76 V. This is similar to the corresponding 20 mV shift observed for the related copper derivative of **2** relative to the related copper derivative of **1**.[78] The nickel(II/I) event of **2** does not shift significantly compared to that of **1**. The $-CH_2CF_3$ functionalities of **3** result in a 160 mV anodic shift of the ligand-centered event to −1.57 V. The nickel(II/I) couple of **3** is similarly shifted to −2.19 V. The magnitude of the shift is in good agreement with Que and co-workers' copper derivatives, which displayed a ∼70 mV anodic shift per $-CF_3$ group compared to CuATSM.[73]

Previously, our laboratory reported the homogeneous HER catalysis of **1**.[77] Under increasing additions of acetic acid in acetonitrile, there was a measurable and stable increase in the catalytic current at −2.35 V versus Fc^+/Fc. This current eventually plateaued, indicating acid saturation. The evolution of hydrogen was confirmed via bulk electrolysis. Overall, as a homogeneous HER catalyst in acetonitrile with acetic acid additions, **1** performed at an overpotential of 0.53 V with turnover frequency and faradaic efficiency values of 4200 s^{-1} and 87%, respectively. The proposed mechanism is a ligand-assisted metal-centered process in which the first reduction occurs on the ligand, followed by protonation on the ligand hydrazino nitrogen atom. Straistari et al. evaluated the *p*-anisole/NiATSM complex for homogeneous HER catalysis, further proving the viability of nickel bis(thiosemicarbazone) complexes for HER catalysis.[25] The bis(thiosemicarbazone) ligand class and metal chelates have been well established for their HER activity.[26,27,68]

HER Activity of Modified Electrodes. Modified electrodes **GC-1**−**GC-3** were prepared by mixing 4 mg of **1**, **2**, or **3** with 1 mL of acetonitrile and 12.5 μL of a 10% aqueous Nafion solution. The resulting suspension was homogenized via ultrasonication, and 10 μL of the suspension was then dropped onto the surface of a GCE. The suspension was allowed to dry on the electrode over rotation at approximately 300 rpm. The freshly prepared modified electrodes required high overpotentials of ~700−750 mV to reach a current density of 10 mA cm^{-2} (the metric for comparing catalysts for water-splitting applications[79,80]) upon immersion in 0.5 M H_2SO_4, indicating poor initial catalytic activity.

The modified electrodes were then conditioned by reductive cycling. The potential was swept between 0 and −0.8 V versus reversible hydrogen electrode (RHE) at 50 mV s^{-1}; electrochemical impedance spectroscopy (EIS) and linear-sweep voltammetry (LSV) at 1 mV s^{-1} over the same potential range were done prior to any cycling and every 100 cycles thereafter to accurately measure the activity of the electrode. It is important to note that chronoamperometry was not used to condition the electrodes, so the activities of the electrodes at various points are quantified after a given number of cycles, not after a certain period of time. For **GC-1**, the overpotential decreases from 0.697 to 0.451 V (Figure 4A). Similarly, the overpotentials for **GC-2** and **GC-3** decrease from 0.703 V to a minimum of 0.446 V and from 0.740 to 0.514 V (parts B and C of Figure 4, respectively). The vertical scale of Figure 4 was truncated at 10 mA cm^{-2} to directly compare the overpotentials required to reach 10 mA cm^{-2}, a commonly used benchmark for water-splitting catalysts. The full ranges of current densities achieved before and after conditioning to the peak activity via cathodic polarization are depicted for **GC-1**−**GC-3** in parts A−C of Figure S6, respectively. The large shift of ~0.250 V represents a dramatic improvement in the catalytic efficiency. Prior to conditioning, the Tafel slopes for **GC-1**−**GC-3** are 91, 72, and 54 mV dec^{-1}, respectively. Following conditioning, for **GC-1** and **GC-2**, the Tafel slopes increase only slightly (Figure 4D,E), suggesting that the mechanism has not significantly changed. The Tafel slope for **GC-3** after reductive cycling did exhibit a significant change (Figure 4F). However, Tafel slopes between 50 and 120 mV dec^{-1} generally indicate a mixed HER mechanism, with proton adsorption being more limiting for higher Tafel slopes.

Extended reductive cycling beyond the point of peak activity was used to probe the stability of **GC-1** − **GC-3**. LSV plots are shown in Figure 5A − 5C respectively and Tafel plots are shown in Figure 5D − 5F respectively. For all three modified electrodes, only minor increases in overpotentials were observed. The relative consistencies of the overpotentials over extended reductive cycling indicates that this class of modified electrodes exhibits high durability for HER catalysis. A comparison of modified electrode performance for **GC-1** − **GC-3** at peak electrochemical activity is summarized in Figure 6. The polarization curves, Figure 6A, show small differences in HER overpotential for **GC-1** − **GC-3**. The Tafel slope plots, Figure 6B, show small differences in the Tafel slopes for **GC-1** − **GC-3** at peak activity.

The effect of organic solvent on the modified electrodes is shown in Figure S7. Modified electrodes **GC-1** and **GC-2**, with and without conditioning through reductive cycling, were immersed in acetonitrile for 30 s while rotating at 800 rpm. Polarization curves were recorded for each modified electrode. After immersion in acetonitrile the conditioned **GC-1** electrode shows greatly diminished HER activity with only slightly lower overpotential compared to a bare GCE (Figure S7A). A similar effect is observed for the conditioned **GC-2** electrode, Figure S7B. Clearly, acetonitrile treatment removes the active catalysts from the electrode. However, the ~100 mV improvement in overpotential (10 mA cm^{-2}) compared to a bare GCE indicates some catalyst remains on the electrode. For a nonconditioned **GC-1** electrode, immersion in acetonitrile (Figure S7C, black trace) actually decrease both the onset potential and the overpotential required to reached a current density of 10 mA cm^{-2}. Attempts to condition the **GC-1** electrode after acetonitrile immersion result in a diminished overpotential (Figure S7, red trace). Similar results are obtained for nonconditioned **GC-2** (Figure S7D). Pretreating the modified electrodes with acetonitrile prior to conditioning may work to roughen the films and expose more active sites for HER. However, the overpotential of the electrodes are ultimately poorer when treating with acetonitrile either before or after conditioning which suggests a net removal of active species from the electrode.

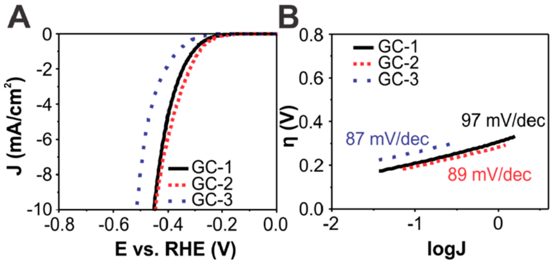

Figure 6. HER performance of three nickel compounds evaluated following reductive cycling to the point of peak catalytic activity. Polarization curves (A) show the onset of hydrogen evolution and the overpotential required for each modified electrode to reach a current density of 10 mA cm^{-2}. Tafel plots (B) show the current response to increasing overpotential throughout the onset period.

Recoverability of the catalysts after conditioning to peak activity is demonstrated in Figure S8. The absorbance spectra of acetonitrile solutions of **2** in various concentrations were measured in Figure S8A and used to construct a calibration curve in Figure S8B. Additionally, **GC-2**, conditioned to 200 cycles, was washed in acetonitrile, and the absorbance spectrum was recorded for the resulting solution. The absorbance spectrum of the recovered material matches those of the acetonitrile solutions of **2**, implying that the chemical structure of the catalyst is retained throughout the conditioning process. From the calibration curve, it was determined that 0.03 mg **2** was recovered from the electrode due to the acetonitrile wash, a recovery of about 75%.

Washing the conditioned modified electrodes in acetonitrile for 30 s results in a substantial loss of activity (blue traces show higher HER overpotential than red traces, Figure S7A,B), consistent with removal of 75% of originally deposited material from the surface. However, the washed electrodes (Figure S7A,B, blue traces) still show lower overpotentials for HER than the bare GCE (Figure S7A,B, black traces), indicating that washing in acetonitrile for 30 s is not sufficient to remove 100% of the catalyst material from the electrode surface. Furthermore, a small amount of catalyst is lost during the conditioning process.

Surface Characterization of Modified Electrodes. To investigate the effect of conditioning by reductive cycling, we visually characterized the surfaces of **GC-1**−**GC-3** using scanning electron microscopy (SEM). Prior to conditioning, the images of **GC-1** (Figure 7A) and **GC-2** (Figure 7B) show similar microcrystalline coatings with boxlike crystals. The

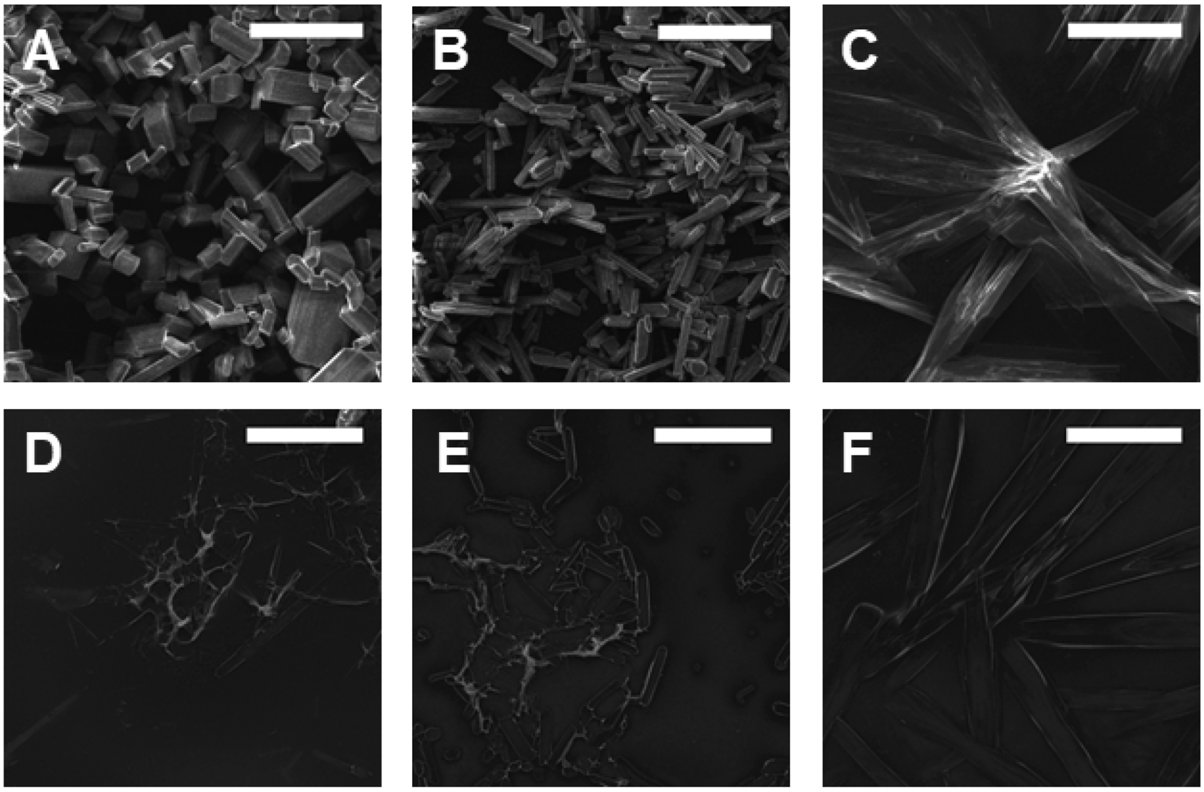

Figure 7. SEM characterization of nickel compound films on GCEs before and after 1000 reductive cycles (0 to −0.8 V vs RHE; 50 mV s^{-1}): (A) **GC-1** before reductive cycling; (B) **GC-2** before reductive cycling; (C) **GC-3** before reductive cycling; (D) **GC-1** after 1000 cycles; (E) **GC-2** after 1000 cycles; (F) **GC-3** after 1000 cycles. All scale bars correspond to 50 μm.

surface morphology of **GC-3** (Figure 7C), while still microcrystalline, has a morphology more akin to thin plates. This difference in the surface morphology is observed in the single crystals investigated by X-ray diffraction (Figure 2). After conditioning to 1000 cycles, the surface of **GC-1** lacks a crystalline appearance and resembles an amorphous microporous network (Figure 7D). A similar trend is observed for **GC-2**. Although the overall boxlike appearance remains intact after 1000 cycles (Figure 7E), there is observable degradation of the crystalline edges and faces. In both cases, conditioning disrupts the crystal packing and reorders the catalyst on the electrode with an increase in the surface area, which results in more exposed active sites. Following conditioning to 1000 cycles, the surface structure of **GC-3** displays a fractured platelike appearance (Figure 7F).

To analyze the retention of the material on the surface of the electrode after cycling to peak activity, a probe Raman system was employed to study modified electrodes and inks of **2**, the best-performing catalyst. Figure S9A shows a spectrum for a GCE with a Nafion film, and Figure S9B shows a spectrum for a bare GCE. This figure shows that Nafion cannot be detected via Raman in the quantities used in this study. Peaks corresponding to glassy carbon are marked with black asterisks. Figure S10A shows a Raman spectrum for acetonitrile, and Figure S10B shows a spectrum for complex **2** in an acetonitrile solution with Nafion. Bands originating from acetonitrile (marked with blue asterisks) are observed in acetonitrile and are retained in the solution of **2**. A total of 10 peaks originating from unique chemical bonds in **2** are observed in Figure S10B and are marked with green asterisks. Figure S10C shows **GC-2** as-deposited. All 10 peaks originating from complex **2** are retained, confirming successful translation of the original complex to the electrode surface. Additionally, bands corresponding to glassy carbon, and some bands corresponding to acetonitrile, are observed. Figure S10D shows **GC-2** after conditioning to peak activity (200 cycles). All 10 peaks originating from **2** are retained, confirming that the original chemical structure of the catalyst is retained throughout the conditioning process.

The modified electrode **GC-2** was selected as a representative sample for surface characterization via energy-dispersive X-ray spectroscopy (EDS) and X-ray photoelectron spectroscopy (XPS) before and after 1000 cycles. EDS studies, performed for both catalyst samples (before and after cycling; Figures S11 and S12, respectively), reveal the presence of nickel and sulfur. Unfortunately, collected EDS data do not provide any information about the local distribution or oxidation state of detected elements. XPS studies were employed to examine the effect of conditioning on speciation of the complexes and to characterize a local distribution on the electrode surface. Survey scans of **GC-2** before and after conditioning to 1000 cycles (Figure S13A) show the presence of a large fluorine signal, attributed to Nafion, before and after conditioning. The survey scan of the bare GCE (Figure S13B) shows that neither nickel nor sulfur is present before dropcasting **2** on the electrode. The atomic compositions of **GC-2** both before and after conditioning are described in Table S5. The peak corresponding to cationic nickel, 853.4 eV[81] (Figure 8A), is identified in the uncycled electrode. The presence of anionic sulfur, 163 eV,[82,83] is concurrently detected in the uncycled electrode (Figure 8B). Fitting parameters for Figure 8A,B can be found in Tables S6 and S7, respectively. To confirm the

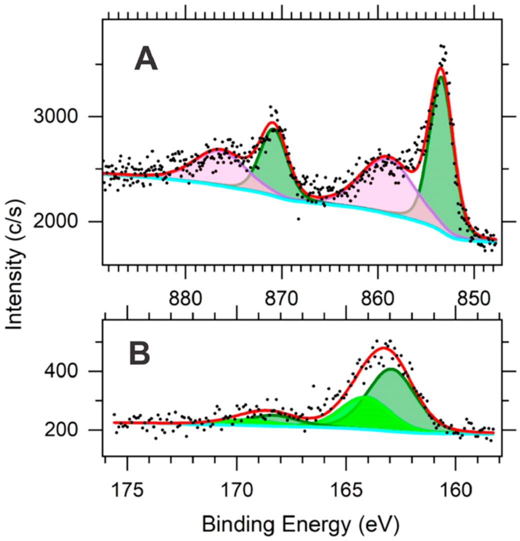

Figure 8. XPS spectra of the cationic nickel region (A) and anionic sulfur region (B) of the uncycled **GC-2** electrode surface. Black dots represent experimental spectra, while the red trace is the generated fit in parts A and B. The green color in part A represents a Ni 2p doublet, the violet color the signal from a F KLL Auger transition, and the cyan color in parts A and B the background. The green and lime colors in part B represent S 2p doublets.

presence of nickel and sulfur, as revealed by EDS, solely occurring from the deposition of our catalyst, secondary X-ray imaging (SXI) and elemental mapping were employed (Figure 9A). The contrast variation observed in SXI is related to lateral distribution of the catalyst (Figure 7) over the electrode surface. The bright-yellow areas correspond to the denser locations of the catalyst, while the dark spots are less covered by the catalyst. The inset of Figure 9A displays a red x in the yellow section and a blue x in the black section. The colors of the x relate to the traces in Figure 9B. In the blue trace, a weak nickel signal is detected; however, the red trace exhibits a distinct nickel signal at 853.4 eV. Elemental mapping of nickel and sulfur seen in Figure 9C follows the location of the bright features seen in SXI (Figure 9A). The green pixels are correlated to Ni $2p_{3/2}$ and the red S 2p (at ~163 eV). A comparison of the elemental mapping with SXI displays that the sulfur and nickel are present at the same location on the electrode surface and only in the areas of dense deposition, indicated by the bright-yellow pixels. Because the bright-yellow pixels are the areas of catalyst deposition, as proven in Figure 9B, we postulate that the observed nickel and sulfur from the elemental mapping (Figure 9C) originates from our catalyst. Formation of NiS during conditioning can be ruled out because NiS is not stable below pH 3,[84] and conditioning takes place in 0.5 M H_2SO_4 (pH 0.3). Nickel sulfides have been reported as catalysts for HER in neutral[85] or alkaline[86] media. Furthermore, no signals for NiS_2,[87] NiS,[88] or Ni_3S_2[89] were detected in the Raman spectrum of **2** in an acetonitrile solution (Figure S10B) or in Raman spectra for **GC-2** before or after conditioning (parts C and D of Figure S10, respectively).

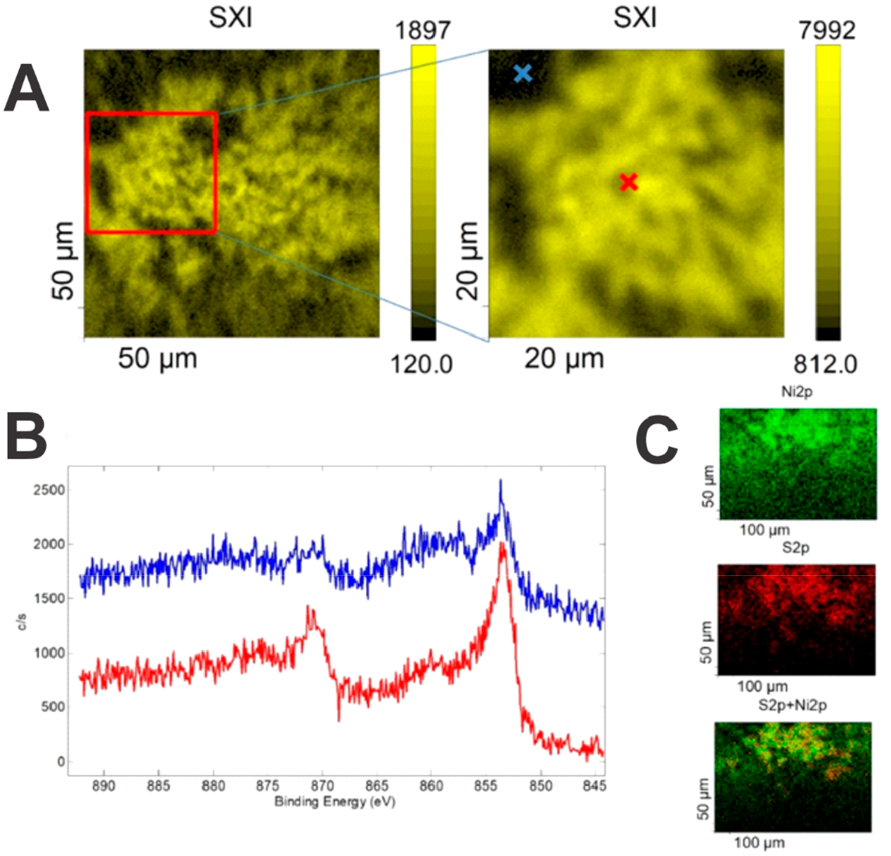

Figure 9. SXI (A) of uncycled **GC-2**, with the inset depicting examined areas and probing points marked by the colored x's for XPS (B), in which the red and blue traces correlate to the red and blue x's, respectively. (C) Elemental mapping (1000 × 700 μm), where nickel is green (top) and sulfur is red (middle) on the electrode. The overlay of the nickel and sulfur maps (bottom) confirms the catalyst location.

DOI: 10.1021/acs.inorgchem.9b01209
Inorg. Chem. 2019, 58, 12025−12039

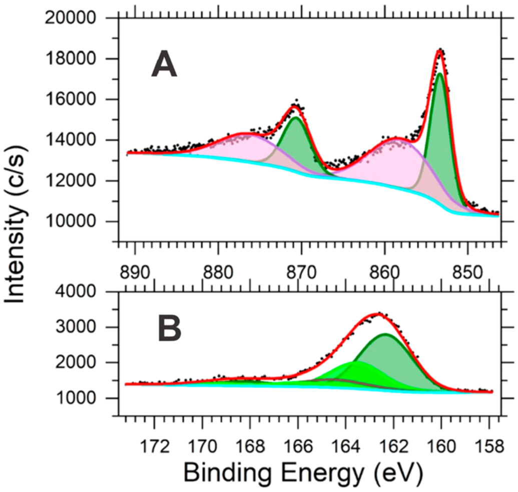

Figure 10. XPS spectra of the cationic nickel region (A) and anionic sulfur region (B) of the cycled **GC-2** electrode surface. The black dots represent experimental spectra in parts A and B, and the red trace is the generated fit. The green color in part A represents a Ni 2p doublet, the violet color the signal from a F KLL Auger transition, and the cyan color the background. The green and lime colors in part B represent S 2p doublets, and the brown color represents elemental sulfur.

After conditioning, the XPS spectra of **GC-2** still display both the cationic nickel (Figure 10A) and anionic sulfur (Figure 10B). The fitting parameters for the respective spectra can be found in Tables S8 and S9. The measured nickel oxidation state after cycling is consistent with its binding energies (BEs) before cycling (Tables S6 and S7). This rules out a noticeable nickel reduction to nickel metal nanoparticles;[90−94] however, nickel oxide nanoparticles with the same Ni 2p BEs cannot be totally ruled out. According to SXI and elemental mapping, we still observe a strong correlation between nickel and sulfur, as distributed on the electrode surface (Figure 11A−C). The red and blue x's in Figure 11A show the locations where data were collected. The red x clearly overlays on the deposited catalyst, whereas the blue x does not. This is substantiated in the XPS spectra for each location (Figure 11B). The red traces of both nickel (top) and sulfur (bottom) display the presence of both elements, whereas there is little to no detection for the blue trace, as seen with the uncycled electrode. Elemental mapping (Figure 11C) confirms that the location of nickel (top) coincides with that of anionic sulfur (middle) when overlaid (bottom). Note that, in order to satisfy the fitting, an additional (to higher sulfur oxidation states seen in the pristine sample) doublet of elemental sulfur (at about of 164 eV) was introduced.

We noticed that the cycling results in a distribution of contrasting features across the scanned area. Consequently, multiple areas on the electrode surface were subjected to elemental mapping using an increased lateral resolution (the scanned areas 200 × 100 vs 1000 × 700 μm), as shown in Figure S14. The data are consistent with observations found for larger scanned areas. The polarization curves (Figure 5) displayed a marginal decrease in the overall activity upon conditioning of the electrode past the point of peak activity, indicative of catalyst loss. The atomic percentage of nickel was determined via XPS, while only a fraction of the C 1s signal related to the C−F bonds in Nafion was included in the calculation. These bonds in Nafion are expected to be the least affected by cycling and the least affected by adventitious carbon contamination, so that the signal was used as a reference. The atomic percentage of nickel in the uncycled electrode was 18%, whereas the cycled compound displayed 13%. The loss of nickel over the conditioning process is consistent with the slight increase in the overpotential (Figure 5B) and Tafel slope (Figure 5E) due to the loss of catalyst from the electrode surface.

EIS was used to study the effect of conditioning on the electrical properties of the modified electrode surface. The impedance data were interpreted using an equivalent circuit model (Figure S15), consisting of the resistance of solution and wires (R_s) in series with an interfacial constant-phase element (CPE) and a charge-transfer resistance (R_c) circuit in parallel along with a Warburg element (W). The CPE is a circuit element used to replace a capacitor and is generally associated with a nonhomogenous surface and variable current density at the electrode. The impedance of the CPE is defined as

$$Z_{\mathrm{CPE}} = (j\omega)^{-n}/Q$$

where Q is the magnitude of the CPE, j is the imaginary unit, ω is the angular frequency, and n is the CPE exponent. The Warburg element was introduced to account for diffusion resistance within the crystalline domains, which are dominant prior to reductive cycling. Details are reported in Table S10.

Prior to conditioning, the Nyquist plots for **GC-1**−**GC-3** (Figures S16−S18, respectively) show large R_c values. The resistance for **GC-3**, 54800 Ω, is larger than those for **GC-1**, 25100 Ω, and **GC-2**, 18800 Ω. Following conditioning, the R_c values for **GC-1**−**GC-3** drop substantially to 270, 160, and 630 Ω, respectively. This dramatic decrease indicates excellent charge-transfer kinetics between the film and electrode attributed to a reorganization of the active sites to improve contact between the electrode and solution. This trend is consistent with the polarization curves in which **GC-3** displayed marginally worse metrics.

To further investigate the electrochemical performances of **GC-1**−**GC-3**, the electrochemical surface areas of the electrodes were approximated via cyclic voltammetry over a potential range where no faradaic processes were observed to occur (0.15−0.35 V vs RHE; Figures S19 and S20). The approximate capacitance was obtained by plotting the average current density at 0.3 V versus RHE as a function of the scan rate and taking the slope (Figures S21 and S22). When the determined capacitances for **GC-1**−**GC-3** are compared to that of GCE, relative roughness factors are obtained, which approximately express the available electrochemical surface area of each modified electrode relative to that of GCE. From this analysis, it was determined that, before conditioning, **GC-1**−**GC-3** have approximately 14, 17, and 8% of the electrochemical surface area of the bare GCE, respectively. However, following conditioning, **GC-1**−**GC-3** all have roughly 400% of the electrochemical surface area of the bare GCE. This evolution of electrode capacitances over the conditioning process suggests that very few active sites are available on the electrodes as deposited, fewer even than on the flat glassy carbon surface. However, the conditioning process exposes more active sites, which likely explains the improvement in the HER activity.

To further probe the surfaces of the modified electrodes, signals for the ferrocyanide/ferricyanide redox couple were

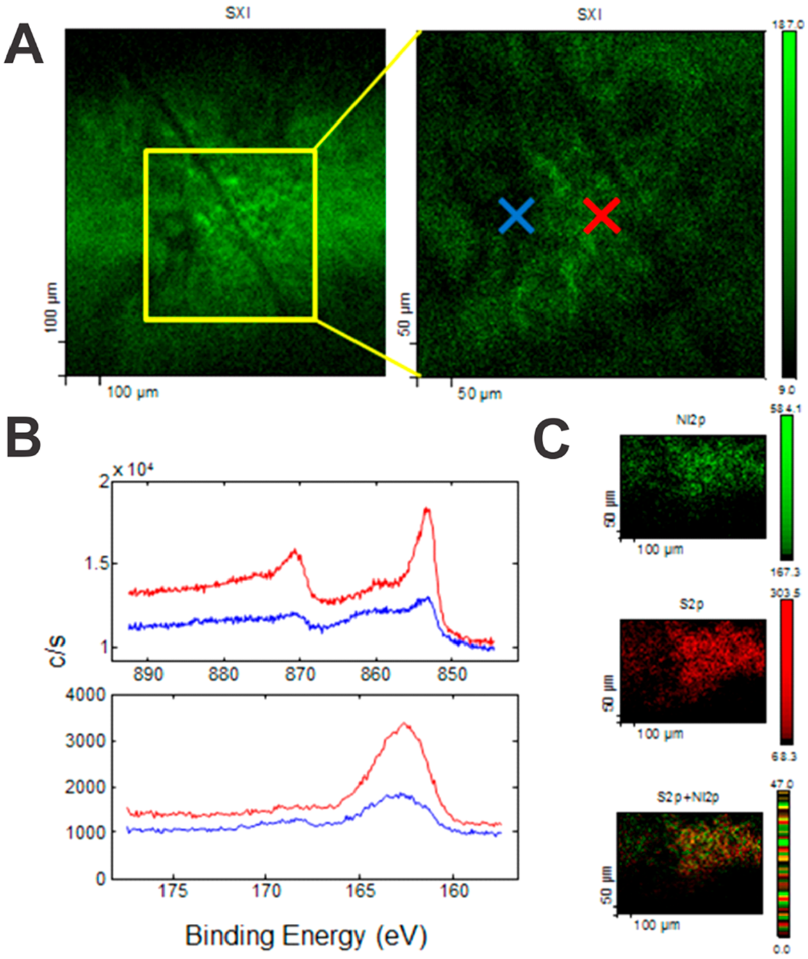

Figure 11. SXI (A) of the **GC-2** electrode after 1000 cycles, with the inset depicting examined areas and probing points marked by the colored x's for XPS (B), in which the red and blue traces correlate to the red and blue x's, respectively. (C) Elemental mapping (1000 × 700 um), where nickel is green (top) and sulfur is red (middle) on the electrode. The overlay image of the nickel and sulfur maps (bottom) confirms the catalyst location.

recorded at various scan rates using the modified electrodes. Oxidation and reduction of the redox couple were observed for **GC-1** as deposited (Figure S23A), **GC-1** after conditioning to 300 cycles (Figure S23B), **GC-2** as deposited (Figure S23C), and **GC-2** after conditioning to 200 cycles (Figure S23D). The maximum (for anodic sweeps) and minimum (for cathodic sweeps) currents were plotted against the square root of the scan rate (Figure S24). The slopes of these traces were used to solve the Randles−Sevcik equation for the electrochemical surface area available for redox of the ferricyanide couple, using previously reported diffusion coefficients.[95] The slopes of the current versus scan rate traces, as well as the calculated surface areas, are presented in Table S11. For both **GC-1** and **GC-2**, the available surface areas increase following the conditioning process. These results appear to indicate a more permeable and accessible catalyst film following conditioning.

Furthermore, **GC-1**−**GC-3** were characterized in terms of the faradaic efficiency (Figure S25). All three modified electrodes exhibited approximately 100% faradaic efficiency. UV−visible (Figure S8) and Raman (Figures S9 and S10) confirm translation of the intact molecular catalyst throughout the dropcasting, drying, and conditioning processes. Conditioning to peak activity produces a more permeable film, as demonstrated by ferrocyanide/ferricyanide experiments (Figures S23 and S24 and Table S11) and the measured capacitances of the modified electrodes (Figures S19−S22). The improvement in the overpotential caused by conditioning is attributed to perforation of the catalytic films by H_2 bubbles, as previously suggested by Konkena et al.[98] XPS studies confirmed the loss of catalyst from the surface during durability studies. Overall, conditioning creates a more open film morphology with more exposed active sites, resulting in improved HER activity up to a certain point. After this point (peak activity), further removal of the catalyst results in decreased activity. In summary, the nature of the catalyst is preserved throughout reductive cycling, and improvements in the HER activity result from H_2 bubbles creating a more permeable film.

The combined surface characterization techniques confirm morphological changes of the catalyst coatings associated with a decrease in *Rc* upon exposure to reductive cycling. For modified electrodes **GC-1** and **GC-2**, conditioning reorganizes the microcrystalline domains as an open-network arrangement, which ostensibly allows for greater solvent access and ion permeability. Despite **GC-3** displaying a different surface morphology, the overall performance is analogous to that of **GC-1** and **GC-2**. We postulate that this dynamic rearrangement gives rise to improved catalytic activity among the three complexes studied here. Minor differences in the catalytic performances of the three complexes are attributed to variations in their crystal-packing schemes.

CONCLUSION

The immobilization of active homogeneous HER catalysts on electrode surfaces has garnered recent attention. A fundamental aspect of these studies is the ability to translate homogeneous solution-phase activity to heterogeneous systems supported on an electrode. In homogeneous systems, the HER activity is largely dependent on the electronic structure of the catalyst, which dictates the reduction potential and interactions with a charged substrate. The physical structure can also be important, as demonstrated in catalysts with pendant amines that help orient the substrate for reduction. However, in heterogeneous systems derived from small-molecule catalysts, the physical structure is an essential component because it relates to catalyst−electrode interactions and charge transfer between the electrode, catalyst, and substrate.

In the current study, electronically similar HER catalysts were translated from homogeneous to heterogeneous solution. A remarkable feature of our system is the good stability of the surface-adhered catalysts without the inclusion of covalent linkers to the surface. The strong stacking interactions observed in the crystal structures lead to robust interactions between the deposited films, dominated by microcrystal domains, and glassy carbon. The noncovalent interactions allow dynamic reorganization upon reductive cycling without changes in the molecular structure of the catalyst. As shown in Scheme 2, initial cycling allows wetting of the catalyst surface and modest hydrogen evolution. The initially evolving hydrogen facilitates loss of crystallinity, leading to additional active sites and decreasing *Rc*. Prolonged reductive cycling leads to a loss of catalyst from the electrode surface and minimally decreases the HER activity. The results demonstrate the translation of a robust homogeneous catalyst to a solid support with no evidence of catalyst degradation or nanoparticle formation.

Scheme 2. Conditioning via Reductive Cycling

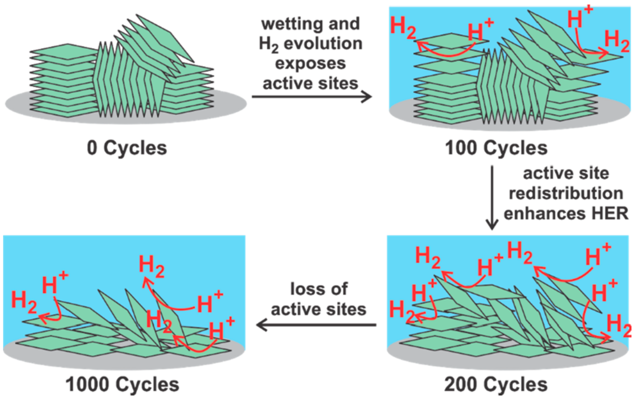

EXPERIMENTAL SECTION

Materials and Reagents. All reagents and solvents were purchased from commercial sources and used as received unless otherwise indicated. Reactions were conducted open to air and under ambient conditions unless otherwise noted. Ni(ATSM),[72] H_2ATSDM,[73] and H_2ATSM-F_6[73] were synthesized according to literature methods. Crystal planarity analysis was done using *PLATON*.[96] All complexes were recrystallized via the evaporation of acetonitrile prior to dropcasting.

Diacetylbis(4,4-dimethyl-3-thiosemicarbazonato)nickel(II) (**2**). The ligand H_2ATSDM (0.28 g, 0.96 mmol) was suspended in methanol (25 mL). To this suspension was added with stirring nickel(II) acetate tetrahydrate (0.25g, 1.0 mmol), immediately giving a color change to a dark-green-brown precipitate. This was stirred at reflux for 4 h. The suspension was allowed to cool to room temperature and then stored in a freezer overnight. The chilled suspension was then filtered cold and washed with water and ethanol, giving a red-brown solid. Yield: 0.29 g (88%). X-ray-quality crystals were obtained by dissolving Ni(ATSDM) in acetonitrile, which was then layered with ether and allowed to slowly evaporate. ^{1}H NMR (C_2D_6SO, 400 MHz): δ 1.87 (s, 3H) 3.10 (s, 6H). IR (cm^{-1}): 2910 (w) and 1501 (s) (CH), 1366 (vs) and 1082 (m) (C−N), 1322 (vs) and 1258 (s) (C═N), 1006 (w) (CS), 900 (m) (NiS), 783 (w) (NiN). Elem anal. Calcd for $C_{10}H_{18}N_6S_2Ni$: C, 34.80; H, 5.26; N, 24.35. Found: C, 34.57; H, 5.20; N, 24.12. MS. Calcd for $C_{10}H_{18}N_6S_2Ni$: *m/z* 344.03878. Found: *m/z* 343.80 (M$^+$), 344.80 (M + H$^+$). UV−visible [acetonitrile; λ_{max}, nm (ε, M^{-1} cm^{-1})]: 256 (23000), 411 (11000), 436 (11000).

Diacetylbis(4-(2,2,2-trifluoroethyl)-3-thiosemicarbazonato)-nickel(II) (**3**). The ligand H_2ATSM-F_6 (0.19 g, 0.48 mmol) was suspended in methanol (20 mL). To this suspension was added with stirring nickel(II) acetate tetrahydrate (0.15, 0.60 mmol), immediately giving a color change to a red-brown precipitate. This was stirred at reflux for 4 h. The suspension was allowed to cool to room temperature and then stored in a freezer overnight. The chilled suspension was then filtered cold and washed with water and ethanol, giving a red-brown solid. Yield: 0.0087 g (40%). X-ray-quality crystals were obtained by dissolving Ni(ATSM-F_6) in acetonitrile, which was then layered with ether and allowed to slowly evaporate. ^{1}H NMR (C_2D_6SO, 400 MHz): δ 1.94 (s, 3H) 4.00 (br, 2H) 8.29 (s, 1H). ^{13}C NMR: δ 178.1, 158.8, 124.9 (q, *J* = 280 Hz), 46.3 (q, *J* = 33 Hz) 14.4. IR (cm^{-1}): 3462 (m) (NH), 1514 (s) and 1476 (s) (CH), 1271 (s) and 1218 (m) (CN), 1138 (vs) (CF), 941 (w) (NiS), 832 (w) (NiN). Elem anal. Calcd for $C_{10}H_{12}N_6S_2F_6Ni$: C, 26.51; H, 2.67; N, 18.55; F, 25.16. Found: C, 26.36; H, 2.59; N, 18.29; F, 25.10. MS. Calcd for $C_{10}H_{18}N_6S_2Ni$: *m/z* 451.9822. Found: *m/z* 452.87 (M + H$^+$). UV−visible [acetonitrile; λ_{max}, nm (ε, M^{-1} cm^{-1})]: 259 (24000), 328 (8200), 392 (9100).

Homogeneous Electrochemical Characterization. Electrochemical data were collected using a Gamry Interface 1000E potentiostat/galvanostat/ZRA. Complexes were dissolved in acetonitrile (1 mM) under air-free conditions in a standard three-electrode cell with 0.1 M TBAHFP as the supporting electrolyte. Glassy carbon was used as the working electrode with a platinum disk counter electrode and a silver wire pseudo reference electrode. Measured potentials were corrected for uncompensated resistance using the current-interrupt function. A small quantity of ferrocene was added as an internal standard, and all potentials are referenced versus Fc$^+$/Fc (ΔE = 63 mV at a scan rate of 50 mV s^{-1}).

Crystallographic Studies. An orange prism 0.40 × 0.34 × 0.18 mm^3 crystal of **2** grown from a solution of acetonitrile and diethyl ether was mounted onto a glass fiber for collection of the X-ray data on an Agilent Technologies/Oxford Diffraction Gemini CCD diffractometer. The *CrysAlisPro*[97] CCD software package (version 1.171.36.32) was used to acquire a total of 1026 20-s frame ω-scan exposures of data at 100 K to a $2\theta_{max}$ = 63.14° using monochromated Mo Kα radiation (0.71073 Å) from a sealed tube. Frame data were processed using *CrysAlisPro*[97] *RED* to determine the final unit cell parameters: a = 7.33437(16) Å, b = 8.5595(2) Å, c = 11.6784(3) Å, α = 103.865(2)°, β = 98.2102(19)°, γ = 91.7205(18)°, V = 702.92(3) Å^3, D_{calc} = 1.631 Mg m^{-3}, and Z = 2 to produce raw *hkl* data that were then corrected for absorption (transmission min/max = 0.778/1.000; μ = 1.672 mm^{-1}) using *SCALE3 ABSPACK*.[98] The structure was solved by direct methods in the space group $P\bar{1}$ using *SHELXS*[99] and refined by least-squares methods on F^2 using *SHELXL*.[99] Non-hydrogen atoms were refined with anisotropic atomic displacement parameters. Hydrogen atoms were located by difference maps and refined isotropically. For all 4702 unique reflections [R(int) = 0.021], the final anisotropic full-matrix least-squares refinement on F^2 for 244 variables converged at R1 = 0.021 and wR2 = 0.055 with a goodness of fit (GOF) of 1.01.

Crystals of **3** suitable for X-ray analysis were grown from an acetonitrile and diethyl ether solution and mounted on a cryoloop for collection of the X-ray data on an Agilent Technologies/Oxford Diffraction Gemini CCD diffractometer. X-ray structural analysis for **3** was performed on a 0.41 × 0.08 × 0.01 mm^3 red-brown plate using a 596-frame, 60-s frame ω-scan data collection strategy at 100 K to $2\theta_{max} = 53.20°$. Complex **3** crystallized in the triclinic space group $P\bar{1}$ with the following unit cell parameters: a = 8.3598(10) Å, b = 9.4027(10) Å, c = 13.5112(17) Å, α = 109.467(10)°, β = 105.475(11)°, γ = 91.382(9)°, V = 957.53(19) $Å^3$, Z = 2, and D_{calc} = 1.571 Mg m^{-3}. A total of 4447 independent data were corrected for absorption (transmission min/max = 0.678/1.000; μ = 1.291 mm^{-1}). The structure was solved by direct methods using *SHELX*.[99] All non-hydrogen atoms were refined with anisotropic atomic displacement parameters. Imine NH hydrogen atoms were located by difference maps and refined isotropically. Methyl hydrogen atoms were placed in their geometrically generated positions and refined as a riding model, and these atoms were assigned as $U(H) = 1.5U_{eq}$. For reflections $I > 2\sigma(I)$ [R(int) = 0.058], the final anisotropic full-matrix least-squares refinement on F^2 for 288 variables converged at R1 = 0.065 and wR2 = 0.119 with a GOF of 1.07.

Heterogeneous Electrochemical Characterization. A 4 mg sample of a given complex was dispersed in 1 mL of acetonitrile (VWR, ACS grade, dried using an MB-SPS from MBRAUN) using a vortex mixer (Vortex Genie 2, Scientific Industries). A 12.5 μL aliquot of a 10% aqueous Nafion solution was added to the resulting ink. The dispersion was further homogenized via ultrasonication (Cole-Parmer ultrasonic bath) for 2 h. After sonication, 10 μL of the resulting dispersion was dropped onto a GCE (E4TQ ChangeDisk, Pine Research), rotating at 50 rpm, affixed to a rotator (MSR Rotator, Pine Research). The rotation speed was subsequently increased to 300 rpm, and this speed was maintained until the film was dried.

Evaluation of the materials' activities for HER was carried out in a three-electrode glass electrochemical cell (RDE/RRDE Cell Without Water Jacket, Pine Research) with 0.5 M H_2SO_4 (VWR, ACS grade) in twice-deionized Millipore water (18.2 Ω cm). A graphite rod (Pine Research), in a protective fritted glass tube (Pine Research), was used as the counter electrode. Ag/AgCl (1 M KCl, CH Instruments) was used as the reference electrode. Measured potentials were calibrated versus RHE after experiments were conducted (to prevent platinum contamination) by measuring the potential difference between a pristine platinum electrode (Standard Platinum Counter Electrode, Pine Research) and the reference electrode in H_2-saturated H_2SO_4. High-purity H_2 and N_2 gases used throughout these experiments were provided by Welders Supply, Louisville, KY.

A Metrohm Autolab PGSTAT302N potentiostat/galvanostat, operating in potentiostat mode, was used to obtain polarization and frequency response analysis (FRA) data. Reductive cycling to activate the catalyst and evaluate its stability was carried out between 0 and −0.8 V versus RHE at 50 mV s^{-1}. LSV was carried out intermittently throughout the cycling process, from 0 to −0.8 V versus RHE at 2 mV s^{-1}, to evaluate the activity of the catalyst, at a relatively high resolution, after various amounts of usage at reductive potentials. FRA data were collected with an applied direct-current bias of −0.3 V versus RHE, starting at 100 kHz and finishing at 0.02 Hz, with 5 mV_{RMS} amplitude. The working electrode was rotated at 800 rpm throughout electrochemical characterization to assist the diffusion of H_2 gas away from the catalyst surface. Measured values were *iR*-compensated by multiplying the measured current at each point by the real component of resistance measured at 100 kHz and then subtracting these values from the corresponding applied potentials.

For determination of the electrochemical surface area, cyclic voltammetry was conducted over the potential range of 0.15−0.35 V versus RHE, where no faradaic processes were observed to occur. Six scan rates were used: 10, 20, 40, 80, 160, and 320 mV s^{-1}. At each vertex (0.15 or 0.35 V vs RHE), a constant potential was maintained for 30 s to allow time for the system to reach a steady state. Three scans were taken for each scan rate, and the measured currents were averaged. The average current at 0.3 V versus RHE during the anodic sweep was plotted as a function of the scan rate. The slope of this curve gives the approximate capacitance of the electrode per geometric surface area. To determine relative electrochemical surface areas, these values were compared to the value obtained for a bare GCE. Ferricyanide redox experiments were carried out in a 0.1 M potassium nitrate and 5 mM potassium ferricyanide solution. The potential was cycled from 0.4 to 1.2 V versus RHE at varying scan rates. Data were taken for each scan rate in triplicate, and measured currents were averaged together. The potential was held at each vertex for 30 s.

For determination of the faradaic efficiencies, produced H_2 gas was measured by gas chromatography (GC; SRI 6810) via online automatic injection (1 mL sample) and a thermal conductivity detector. Nitrogen (99.99%, Specialty Gases) was used as the carrier gas to enable accurate H_2 quantification. The gas was injected every 15 min, and each measured value for the faradaic efficiency was representative of the past 15 min of electrolysis. In the bulk electrolysis cell itself, nitrogen was diffused into the electrolyte at 10 sccm regulated by a mass flow controller (MKS Instruments, Inc.). The potentiostat was operated in galvanostatic mode at a constant current density of 10 mA cm^{-2} during faradaic efficiency measurements. The electrochemical cell was set up identically as described for all other heterogeneous electrochemical experiments except the joints were sealed with vacuum grease and an air outlet line was run from the cell to the GC apparatus. In order to maintain an airtight seal, the GCE was not rotated. Instead, a magnetic stirrer was rotated at 360 rpm underneath the GCE to remove H_2 bubbles from the electrode surface. Theoretical H_2 was determined by counting the coulombs of charge that passed, and measured H_2 was determined via GC. The faradaic efficiencies were determined by comparing these values.

XPS. The XPS experiments were carried out using a PHI *VersaProbe* II instrument equipped with a focused monochromatic Al Kα source. The instrument base pressure was ca. 8 × 10^{-10} Torr. An X-ray power of 25 W at 15 kV was used for the XPS spectral acquisition mode with a 100 μm beam size at an X-ray incidence and takeoff angle of 45°. Calibration of the instrument work function was set to give a BE of 84.0 eV for the Au $4f_{7/2}$ line for metallic gold. The spectrometer dispersion was adjusted to give BEs of 284.8, 932.7, and 368.3 eV for the C 1s line of adventitious (aliphatic) carbon presented on the nonsputtered sample, Cu $2p_{3/2}$ and Ag $3d_{5/2}$, photoemission lines, respectively. The PHI dual-charge neutralization system was used on all samples. The high-resolution Ni 2p, N 1s, O 1s, C 1s, and S 2p spectra were taken with a minimum of 10−60 s scans using 0.1 eV steps and 93.9, 46.95, 23.5, and 93.9 eV pass energy, respectively. MultiPak version 9.3.0.3, PHI software was used for signal above background measurement and Shirley background subtraction. At the ultimate PHI *Versa Probe* II instrumental resolution, the temperature spread (at 14/86%) of the metallic silver Fermi edge was less than 120 meV. All XPS spectra were recorded using the PHI software SmartSoft−VP Version 2.6.3.4, and processed using MultiPak Version 9.3.0.3, and/or *CasaXPS*, version 2.3.14. The relative sensitivity factors from the MultiPack library were used to determine atomic percentages. Peaks were fitted using GL line shapes, a combination of Gaussians and Lorentzians. A given sample was examined at five or six different spots on the mounted specimen to ensure that consistent, reproducible results were obtained. Elemental mapping of the 1000 × 700 and 200 × 100 μm areas was acquired with a FAT analyzer mode using 0.2 eV steps and 187.85 eV pass energy. X-ray beam sizes of 35 and 9 μm were used for the 1000 × 700 and 200 × 100 μm areas, respectively. The last image was constructed of 133 × 66 pixels.

Other Characterization. SEM was carried out using a TESCAN VEGA3 microscope operating at 10 kV and 10 mA. Images of the catalyst materials were taken using the ejectable GCE disk tip as the substrate. As above, catalyst dispersion was dropped onto the GCE and allowed to dry over rotation. At this point, either the disk was ejected and taken to the SEM or the material was cycled to peak activity (as described above) before disk ejection and characterization. EDS characterization was carried out concurrently with SEM studies using an energy-dispersive X-ray analysis system attached to the electron microscope. EDS studies were done at 20 kV with a 50 nm spot size on the deposited film. The beam current was increased until the detector registered approximately 1000 counts s^{-1}. Consistent spectra were obtained for various spots.

Raman spectra from 100 to 3200 cm^{-1} were collected with a Reva Educational Raman spectrometer (Hellma USA, Inc., Plainview, NY). Samples were excited with a 450 mW collimated laser beam at 785 nm, and spectra were obtained by averaging 10 scans with a 400 ms integration time per scan. Electrode samples were prepared for Raman, as described for SEM. Acetonitrile inks with complex **2** and Nafion were evaluated as-prepared using the probe Raman spectrometer. Acetonitrile and glassy carbon were each directly measured using the probe Raman spectrometer. A modified electrode with Nafion was prepared by dropcasting 10 μL of an acetonitrile solution with the same Nafion content as that described for the catalytic inks but without a complex onto a GCE.

UV−visible spectroscopy was carried out using an Agilent Technologies Cary 60 UV−visible spectrometer. Standard solutions of **2** were prepared via serial dilution from the original 4 mg mL^{-1} acetonitrile ink with Nafion and used to construct a calibration curve. The peak at 260 nm was chosen for quantification because it was the most intense. **GC-2** was conditioned to peak activity (200 cycles) in sulfuric acid as previously described, washed thoroughly with deionized water, and immersed in 3 mL of acetonitrile for 30 s over rotation at 800 rpm. The resulting yellow acetonitrile solution was evaluated via UV−visible, and its absorbance was used to interpolate the solution concentration based upon the calibration curve.

■ ASSOCIATED CONTENT

Ⓢ Supporting Information

The Supporting Information is available free of charge on the ACS Publications website at DOI: 10.1021/acs.inorgchem.9b01209.

> NMR, FT-IR, and UV−visible spectra, crystal data and structural refinement details for **2** and **3** with tables of selected bond distances and bond angles, SEM image of **GC-2**, Raman spectra, additional polarization curves, circuit model, FRA parameters, and Nyquist plots, faradaic efficiency plots, electrochemical surface area plots, and additional Tafel plots (PDF)

Accession Codes

CCDC 1866543 and 1866544 contain the supplementary crystallographic data for this paper. These data can be obtained free of charge via www.ccdc.cam.ac.uk/data_request/cif, or by emailing data_request@ccdc.cam.ac.uk, or by contacting The Cambridge Crystallographic Data Centre, 12 Union Road, Cambridge CB2 1EZ, UK; fax: +44 1223 336033.

■ AUTHOR INFORMATION

Corresponding Authors

*E-mail: gautam.gupta@louisville.edu.
*E-mail: craig.grapperhaus@louisville.edu.

ORCID

Joshua Spurgeon: 0000-0002-2987-0865
Craig A. Grapperhaus: 0000-0003-4889-2645

Author Contributions

[§]The manuscript was written through contributions of all authors. All authors have given approval to the final version of the manuscript. These authors contributed equally.

Notes

The authors declare no competing financial interest.

■ ACKNOWLEDGMENTS

This research was supported, in part, by National Science Foundation Grants CHE-1665136 (to C.A.G.) and CHE-1800245 (to G.G. and R.M.B.). M.S.M. thanks the Department of Energy (Grant DEFG02-08CH11538) and the Kentucky Research Challenge Trust Fund for an upgrade of our X-ray facilities.

■ REFERENCES

(1) Hoffert, M. I.; Caldeira, K.; Jain, A. K.; Haites, E. F.; Harvey, L. D. D.; Potter, S. D.; Schlesinger, M. E.; Schneider, S. H.; Watts, R. G.; Wigley, T. M. L.; Wuebbles, D. J. Energy implications of future stabilization of atmospheric CO_2 content. *Nature* **1998**, *395*, 881−884.

(2) Lewis, N. S.; Nocera, D. G. Powering the planet: Chemical challenges in solar energy utilization. *Proc. Natl. Acad. Sci. U. S. A.* **2006**, *103*, 15729−15735.

(3) Park, J. H.; Kim, S.; Bard, A. J. Novel carbon-doped TiO_2 nanotube arrays with high aspect ratios for efficient solar water splitting. *Nano Lett.* **2006**, *6*, 24−28.

(4) Khaselev, O.; Turner, J. A. A monolithic photovoltaic-photoelectrochemical device for hydrogen production via water splitting. *Science* **1998**, *280*, 425−427.

(5) Kim, T. W.; Choi, K.-S. Nanoporous $BiVO_4$ photoanaodes with dual-layer oxygen evolution catalysts for solar water splitting. *Science* **2014**, *343*, 990−994.

(6) Sivula, K.; LeFormal, F.; Grätzel, M. Solar water splitting: Progress using hematite (α-Fe_2O_3) photoelectrodes. *ChemSusChem* **2011**, *4*, 432−449.

(7) Turner, J. A. A realizable renewable energy future. *Science* **1999**, *285*, 687−689.

(8) Crabtree, G. W.; Dresselhaus, M. S.; Buchanan, M. V. The hydrogen economy. *Phys. Today* **2004**, *57*, 39−44.

(9) Kibler, L. A. Hydrogen electrocatalysis. *ChemPhysChem* **2006**, *7*, 985−991.

(10) Subbaraman, R.; Tripkovic, D.; Strmcnik, D.; Chang, K.-C.; Uchimura, M.; Paulikas, A. P.; Stamenkovic, V.; Markovic, N. M. Enhancing hydrogen evolution activity in water splitting by tailoring Li^+-$Ni(OH)_2$-Pt interfaces. *Science* **2011**, *334*, 1256−1260.

(11) Di Giovanni, C.; Wang, W.-A.; Nowak, S.; Grenèche, J.-M.; Lecoq, H.; Mouton, L.; Giraud, M.; Tard, C. Bioinspired iron sulfide nanoparticles for cheap and long-lived electrocatalytic molecular hydrogen evolution in neutral water. *ACS Catal.* **2014**, *4*, 681−687.

(12) Popczun, E. J.; Read, C. G.; Roske, C. W.; Lewis, N. S.; Schaak, R. E. Highly active electrocatalysis of the hydrogen evolution reaction by cobalt phosphide nanoparticles. *Angew. Chem., Int. Ed.* **2014**, *53*, 5427−5430.

(13) Tang, C. P. Z.; Pu, Z.; Liu, Q.; Asiri, A. M.; Sun, X. NiS_2 nanosheets array grown on carbon cloth as an efficient 3D hydrogen evolution cathode. *Electrochim. Acta* **2015**, *153*, 508−514.

(14) Tian, J.; Liu, Q.; Cheng, N.; Asiri, A. M.; Sun, X. Self-supported Cu_3P nanowire arrays as an integrated high-performance three-dimensional cathode for generating hydrogen from water. *Angew. Chem., Int. Ed.* **2014**, *53*, 9577−9581.

(15) Ye, G.; Gong, Y.; Lin, J.; Li, B.; He, Y.; Pantelides, S. T.; Zhou, W.; Vajtai, R.; Ajayan, P. M. Defects engineered monolayer MoS_2 for improved hydrogen evolution reaction. *Nano Lett.* **2016**, *16*, 1097−1103.

(16) Li, Y.; Wang, H.; Xie, L.; Liang, Y.; Hong, G.; Dai, H. MoS_2 nanoparticles grown on graphene: An advanced catalyst for the hydrogen evolution reaction. *J. Am. Chem. Soc.* **2011**, *133*, 7296−7299.

(17) Yan, Y.; Xia, B.; Xu, Z.; Wang, X. Recent development of molybdenum sulfides as advanced electrocatalysts for hydrogen evolution reaction. *ACS Catal.* **2014**, *4*, 1693−1705.

(18) Popczun, E. J.; McKone, J. R.; Read, C. G.; Biacchi, A. J.; Wiltrout, A. M.; Lewis, N. S.; Schaak, R. E. Nanostructured nickel

phosphide as an electrocatalyst for the hydrogen evolution reaction. *J. Am. Chem. Soc.* **2013**, *135*, 9267−9270.

(19) Kong, D.; Cha, J. J.; Wang, H.; Lee, H. R.; Cui, Y. First-row transition metal dichalcogenide catalysts for hydrogen evolution reaction. *Energy Environ. Sci.* **2013**, *6*, 3553−3558.

(20) Bonde, J.; Moses, P. G.; Jaramillo, T. F.; Nørskov, J. K.; Chorkendorff, I. Hydrogen evolution on nano-particulate transition metal sulfides. *Faraday Discuss.* **2009**, *140*, 219−231.

(21) Merki, D.; Hu, X. Recent developments of molybdenum and tungsten sulfides as hydrogen evolution catalysts. *Energy Environ. Sci.* **2011**, *4*, 3878−3888.

(22) Rountree, E. S.; Dempsey, J. L. Reactivity of proton sources with a nickel hydride complex in acetonitrile: Implications for the study of fuel-forming catalysts. *Inorg. Chem.* **2016**, *55*, 5079−5087.

(23) Dempsey, J. L.; Brunschwig, B. S.; Winkler, J. R.; Gray, H. B. Hydrogen evolution catalyzed by cobaloximes. *Acc. Chem. Res.* **2009**, *42*, 1995−2004.

(24) Mejia-Rodriguez, R.; Chong, D.; Reibenspies, J. H.; Soriaga, M. P.; Darensbourg, M. Y. The hydrophilic phosphatriazaadamantane ligand in the development of H_2 production electrocatalysts: Iron hydrogenase model complexes. *J. Am. Chem. Soc.* **2004**, *126*, 12004−12014.

(25) Straistari, T.; Fize, J.; Shova, S.; Réglier, M.; Artero, V.; Orio, M. A thiosemicarbazone−nickel(II) complex as efficient electrocatalyst for hydrogen evolution. *ChemCatChem* **2017**, *9*, 2262−2268.

(26) Haddad, A. Z.; Cronin, S. P.; Mashuta, M. S.; Buchanan, R. M.; Grapperhaus, C. A. Metal-assisted ligand-centered electrocatalytic hydrogen evolution upon reduction of a bis(thiosemicarbazonato)-Cu(II) complex. *Inorg. Chem.* **2017**, *56*, 11254−11265.

(27) Straistari, T.; Hardre, R.; Massin, J.; Attolini, M.; Faure, B.; Giorgi, M.; Reglier, M.; Orio, M. Influence of the metal ion on the electrocatalytic hydrogen production by a thiosemicarbazone palladium complex. *Eur. J. Inorg. Chem.* **2018**, *2018*, 2259−2266.

(28) Haddad, A. Z.; Kumar, D.; Ouch Sampson, K.; Matzner, A. M.; Mashuta, M. S.; Grapperhaus, C. A. Proposed ligand-centered electrocatalytic hydrogen evolution and hydrogen oxidation at a noninnocent mononuclear metal−thiolate. *J. Am. Chem. Soc.* **2015**, *137*, 9238−9241.

(29) Merki, D.; Vrubel, H.; Rovelli, L.; Fierro, S.; Hu, X. Fe, Co, and Ni ions promote the catalytic activity of amorphous molybdenum sulfide films for hydrogen evolution. *Chem. Sci.* **2012**, *3*, 2515−2525.

(30) Xiao, P.; Sk, M. A.; Thia, L.; Ge, X.; Lim, R. J.; Wang, J.-Y.; Lim, K. H.; Wang, X. Molybdenum phosphide as an efficient electrocatalyst for the hydrogen evolution reaction. *Energy Environ. Sci.* **2014**, *7*, 2624−2629.

(31) Jaramillo, T. F.; Jørgensen, K. P.; Bonde, J.; Nielsen, J. H.; Horch, S.; Chorkendorff, I. Identification of active edge sites for electrochemical H_2 evolution from MoS_2 nanocatalysts. *Science* **2007**, *317*, 100−102.

(32) Popczun, E. J.; McKone, J. R.; Read, C. G.; Biacchi, A. J.; Wiltrout, A. M.; Lewis, N. S.; Schaak, R. E. Nanostructured nickel phosphide as an electrocatalyst for the hydrogen evolution reaction. *J. Am. Chem. Soc.* **2013**, *135*, 9267−9270.

(33) Callejas, J. F.; McEnaney, J. M.; Read, C. G.; Crompton, J. C.; Biacchi, A. J.; Popczun, E. J.; Gordon, T. R.; Lewis, N. S.; Schaak, R. E. Electrocatalytic and photocatalytic hydrogen production from acidic and neutral-pH aqueous solutions using iron phosphide nanoparticles. *ACS Nano* **2014**, *8*, 11101−11107.

(34) Chen, W. F.; Sasaki, K.; Ma, C.; Frenkel, A. I.; Marinkovic, N.; Muckerman, J. T.; Zhu, Y.; Adzic, R. R. Hydrogen-evolution catalysts based on non-noble metal nickel−molybdenum nitride nanosheets. *Angew. Chem., Int. Ed.* **2012**, *51*, 6131−6135.

(35) Lazarides, T.; McCormick, T.; Du, P.; Luo, G.; Lindley, B.; Eisenberg, R. Hydrogen from water using a homogeneous system without noble metals. *J. Am. Chem. Soc.* **2009**, *131*, 9192−9194.

(36) Fukuzumi, S.; Yamada, Y.; Suenobu, T.; Ohkubo, K.; Kotani, H. Catalytic mechanisms of hydrogen evolution with homogeneous and heterogeneous catalysts. *Energy Environ. Sci.* **2011**, *4*, 2754−2766.

(37) Ford, P. C. The water gas shift reaction: Homogeneous catalysis by ruthenium and other metal carbonyls. *Acc. Chem. Res.* **1981**, *14*, 31−37.

(38) Rakowski DuBois, M.; DuBois, D. L. Development of molecular electrocatalysts for CO_2 reduction and H_2 production/oxidation. *Acc. Chem. Res.* **2009**, *42*, 1974−1982.

(39) Wiese, S.; Kilgore, U. J.; DuBois, D. L.; Bullock, R. M. $[Ni(PMe_2NPh_2)_2](BF_4)_2$ as an electrocatalyst for H_2 production. *ACS Catal.* **2012**, *2*, 720−727.

(40) Brown, A. P.; Anson, F. C. Molecular anchors for the attachment of metal complexes to graphite electrode surfaces. *J. Electroanal. Chem. Interfacial Electrochem.* **1977**, *83*, 203−206.

(41) Bullock, R. M.; Das, A. K.; Appel, A. M. Surface immobilization of molecular electrocatalysts for energy conversion. *Chem. - Eur. J.* **2017**, *23*, 7626−7641.

(42) Blakemore, J. D.; Gupta, A.; Warren, J. J.; Brunschwig, B. S.; Gray, H. B. Noncovalent immobilization of electrocatalysts on carbon electrodes for fuel production. *J. Am. Chem. Soc.* **2013**, *135*, 18288−18291.

(43) Mann, J. A.; Rodríguez-López, J.; Abruña, H. D.; Dichtel, W. R. Multivalent binding motifs for the noncovalent functionalization of graphene. *J. Am. Chem. Soc.* **2011**, *133*, 17614−17617.

(44) Le Goff, A.; Artero, V.; Jousselme, B.; Tran, P. D.; Guillet, N.; Métayé, R.; Fihri, A.; Palacin, S.; Fontecave, M. From hydrogenases to noble metal−free catalytic nanomaterials for H_2 production and uptake. *Science* **2009**, *326*, 1384−1387.

(45) Pantani, O.; Anxolabéhère-Mallart, E.; Aukauloo, A.; Millet, P. Electroactivity of cobalt and nickel glyoximes with regard to the electro-reduction of protons into molecular hydrogen in acidic media. *Electrochem. Commun.* **2007**, *9*, 54−58.

(46) Berben, L. A.; Peters, J. C. Hydrogen evolution by cobalt tetraimine catalysts adsorbed on electrode surfaces. *Chem. Commun.* **2010**, *46*, 398−400.

(47) Lei, H.; Han, A.; Li, F.; Zhang, M.; Han, Y.; Du, P.; Lai, W.; Cao, R. Electrochemical, spectroscopic and theoretical studies of a simple bifunctional cobalt corrole catalyst for oxygen evolution and hydrogen production. *Phys. Chem. Chem. Phys.* **2014**, *16*, 1883−1893.

(48) Mondal, B.; Sengupta, K.; Rana, A.; Mahammed, A.; Botoshansky, M.; Dey, S. G.; Gross, Z.; Dey, A. Cobalt corrole catalyst for efficient hydrogen evolution reaction from H_2O under ambient conditions: Reactivity, spectroscopy, and density functional theory calculations. *Inorg. Chem.* **2013**, *52*, 3381−3387.

(49) Rodriguez-Macia, P.; Priyadarshani, N.; Dutta, A.; Weidenthaler, C.; Lubitz, W.; Shaw, W. J.; Rudiger, O. Covalent attachment of the water-insoluble $Ni(PCy_2NPhe_2)_2$ electrocatalyst to electrodes showing reversible catalysis in aqueous solution. *Electroanalysis* **2016**, *28*, 2452−2458.

(50) Oughli, A. A.; Ruff, A.; Boralugodage, N. P.; Rodríguez-Maciá, P.; Plumeré, N.; Lubitz, W.; Shaw, W. J.; Schuhmann, W.; Rüdiger, O. Dual properties of a hydrogen oxidation Ni-catalyst entrapped within a polymer promote self-defense against oxygen. *Nat. Commun.* **2018**, *9*, 864−869.

(51) Tran, P. D.; LeGoff, A.; Heidkamp, J.; Jousselme, B.; Guillet, N.; Palacin, S.; Dau, H.; Fontecave, M.; Artero, V. Noncovalent modification of carbon nanotubes with pyrene-functionalized nickel complexes: Carbon monoxide tolerant catalysts for hydrogen evolution and uptake. *Angew. Chem.* **2011**, *123*, 1407−1410.

(52) Zhang, W.; Haddad, A. Z.; Garabato, B. D.; Kozlowski, P. M.; Buchanan, R. M.; Grapperhaus, C. A. Translation of ligand-centered hydrogen evolution reaction activity and mechanism of a rhenium-thiolate from solution to modified electrodes: A combined experimental and density functional theory study. *Inorg. Chem.* **2017**, *56*, 2177−2187.

(53) Abe, T.; Taguchi, F.; Imaya, H.; Zhao, F.; Zhang, J.; Kaneko, M. Highly active electrocatalysis by cobalt tetraphenylporphyrin incorporated in a Nafion membrane for proton reduction. *Polym. Adv. Technol.* **1998**, *9*, 559−562.

(54) Koca, A. Copper phthalocyanine complex as electrocatalyst for hydrogen evolution reaction. *Electrochem. Commun.* **2009**, *11*, 838−841.

(55) Koca, A.; Kalkan, A.; Altuntaş Bayır, Z. Electrochemical, insitu spectroelectrochemical, in situ electrocolorimetric and electrocatalytic characterization of metallophthalocyanines bearing four dioctylaminocarbonyl biphenyloxy substituents. *Electroanalysis* **2010**, *22*, 310−319.

(56) Koca, A.; Kalkan, A.; Bayır, Z. A. Electrocatalytic oxygen reduction and hydrogen evolution reactions on phthalocyanine modified electrodes: Electrochemical, *in situ* spectroelectrochemical, and *in situ* electrocolorimetric monitoring. *Electrochim. Acta* **2011**, *56*, 5513−5525.

(57) Koca, A. Hydrogen evolution reaction on glassy carbon electrode modified with titanyl phthalocyanines. *Int. J. Hydrogen Energy* **2009**, *34*, 2107−2112.

(58) Grass, V.; Lexa, D.; Savéant, J.-M. Electrochemical generation of rhodium porphyrin hydrides. Catalysis of hydrogen evolution. *J. Am. Chem. Soc.* **1997**, *119*, 7526−7532.

(59) Anxolabehere-Mallart, E.; Costentin, C.; Fournier, M.; Robert, M. Cobalt-bisglyoximato diphenyl complex as a precatalyst for electrocatalytic H_2 evolution. *J. Phys. Chem. C* **2014**, *118*, 13377−13381.

(60) El Ghachtouli, S.; Fournier, M.; Cherdo, S. p.; Guillot, R. g.; Charlot, M.-F.; Anxolabéhère-Mallart, E.; Robert, M.; Aukauloo, A. Monometallic cobalt−trisglyoximato complexes as precatalysts for catalytic H_2 evolution in water. *J. Phys. Chem. C* **2013**, *117*, 17073−17077.

(61) Anxolabéhère-Mallart, E.; Costentin, C.; Fournier, M.; Nowak, S.; Robert, M.; Savéant, J.-M. Boron-capped tris (glyoximato) cobalt clathrochelate as a precursor for the electrodeposition of nanoparticles catalyzing H_2 evolution in water. *J. Am. Chem. Soc.* **2012**, *134*, 6104−6107.

(62) Cherdo, S.; El Ghachtouli, S.; Sircoglou, M.; Brisset, F.; Orio, M.; Aukauloo, A. A nickel dimethyl glyoximato complex to form nickel based nanoparticles for electrocatalytic H_2 production. *Chem. Commun.* **2014**, *50*, 13514−13516.

(63) Fang, M.; Engelhard, M. H.; Zhu, Z.; Helm, M. L.; Roberts, J. A. Electrodeposition from acidic solutions of nickel bis (benzenedithiolate) produces a hydrogen-evolving Ni−S film on glassy carbon. *ACS Catal.* **2014**, *4*, 90−98.

(64) Martin, D. J.; McCarthy, B. D.; Donley, C. L.; Dempsey, J. L. Electrochemical hydrogenation of a homogeneous nickel complex to form a surface adsorbed hydrogen-evolving species. *Chem. Commun.* **2015**, *51*, 5290−5293.

(65) McCarthy, B. D.; Donley, C. L.; Dempsey, J. L. Electrode initiated proton-coupled electron transfer to promote degradation of a nickel(II) coordination complex. *Chem. Sci.* **2015**, *6*, 2827−2834.

(66) Wombwell, C.; Reisner, E. Synthesis, structure and reactivity of Ni site models of [NiFeSe] hydrogenases. *Dalton Trans* **2014**, *43*, 4483−4493.

(67) Jurss, J. W.; Khnayzer, R. S.; Panetier, J. A.; El Roz, K. A.; Nichols, E. M.; Head-Gordon, M.; Long, J. R.; Castellano, F. N.; Chang, C. J. Bioinspired design of redox-active ligands for multielectron catalysis: Effects of positioning pyrazine reservoirs on cobalt for electro- and photocatalytic generation of hydrogen from water. *Chem. Sci.* **2015**, *6*, 4954−4972.

(68) Haddad, A. Z.; Garabato, B. D.; Kozlowski, P. M.; Buchanan, R. M.; Grapperhaus, C. A. Beyond metal-hydrides: Non-transition-metal and metal-free ligand-centered electrocatalytic hydrogen evolution and hydrogen oxidation. *J. Am. Chem. Soc.* **2016**, *138*, 7844−7847.

(69) Thompson, E. J.; Berben, L. A. Electrocatalytic hydrogen production by an aluminum(III) complex: Ligand-based proton and electron transfer. *Angew. Chem., Int. Ed.* **2015**, *54*, 11642−11646.

(70) Sherbow, T. J.; Fettinger, J. C.; Berben, L. A. Control of ligand pK_a values tunes the electrocatalytic dihydrogen evolution mechanism in a redox-active aluminum(III) complex. *Inorg. Chem.* **2017**, *56*, 8651−8660.

(71) Panetier, J. A.; Letko, C. S.; Tilley, T. D.; Head-Gordon, M. Computational characterization of redox non-innocence in cobalt-bis(diaryldithiolene)-catalyzed proton reduction. *J. Chem. Theory Comput.* **2016**, *12*, 223−230.

(72) West, D. X.; Ives, J. S.; Bain, G. A.; Liberta, A. E.; Valdés-Martínez, J.; Ebert, K. H.; Hernández-Ortega, S. Copper(II) and nickel(II) complexes of 2,3-butanedione bis(N(3)-substituted thiosemicarbazones). *Polyhedron* **1997**, *16*, 1895−1905.

(73) Xie, D.; King, T. L.; Banerjee, A.; Kohli, V.; Que, E. L. Exploiting copper redox for ^{19}F magnetic resonance-based detection of cellular hypoxia. *J. Am. Chem. Soc.* **2016**, *138*, 2937−2940.

(74) Blower, P. J.; Castle, T. C.; Cowley, A. R.; Dilworth, J. R.; Donnelly, P. S.; Labisbal, E.; Sowrey, F. E.; Teat, S. J.; Went, M. J. Structural trends in copper(II) bis(thiosemicarbazone) radiopharmaceuticals. *Dalton Trans* **2003**, *23*, 4416−4425.

(75) Farrugia, L. ORTEP-3 for Windows - a version of ORTEP-III with a graphical user interface (GUI). *J. Appl. Crystallogr.* **1997**, *30*, 565.

(76) Vishnosky, N. S.; Mashuta, M. S.; Buchanan, R. M.; Grapperhaus, C. A. Syntheses, structures, and electrochemical studies of *N,N'*-bis(alkylthiocarbamate) butane-2,3-diimine Cu(II) complexes as pendent alkoxy derivatives of Cu(ATSM). *Inorg. Chim. Acta* **2017**, *461*, 45−51.

(77) Jain, R.; Mamun, A. A.; Buchanan, R. M.; Kozlowski, P. M.; Grapperhaus, C. A. Ligand-assisted metal-centered electrocatalytic hydrogen evolution upon reduction of a bis(thiosemicarbazonato)-Ni(II) complex. *Inorg. Chem.* **2018**, *57*, 13486−13493.

(78) Dearling, J. L.; Lewis, J. S.; Mullen, G. E.; Welch, M. J.; Blower, P. J. Copper bis(thiosemicarbazone) complexes as hypoxia imaging agents: structure-activity relationships. *JBIC, J. Biol. Inorg. Chem.* **2002**, *7*, 249−259.

(79) Walter, M. G.; Warren, E. L.; McKone, J. R.; Boettcher, S. W.; Mi, Q.; Santori, E. A.; Lewis, N. S. Solar water splitting cells. *Chem. Rev.* **2010**, *110*, 6446−6473.

(80) Weber, M. F.; Dignam, M. J. Efficiency of splitting water with semiconducting photoelectrodes. *J. Electrochem. Soc.* **1984**, *131*, 1258−1265.

(81) Dickinson, T.; Povey, A. F.; Sherwood, P. M. Dissolution and passivation of nickel. An X-ray photoelectron spectroscopic study. *J. Chem. Soc., Faraday Trans. 1* **1977**, *73*, 327−343.

(82) Descostes, M.; Mercier, F.; Thromat, N.; Beaucaire, C.; Gautier-Soyer, M. Use of XPS in the determination of chemical environment and oxidation state of iron and sulfur samples: constitution of a data basis in binding energies for Fe and S reference compounds and applications to the evidence of surface species of an oxidized pyrite in a carbonate medium. *Appl. Surf. Sci.* **2000**, *165*, 288−302.

(83) Peisert, H.; Chassé, T.; Streubel, P.; Meisel, A.; Szargan, R. Relaxation energies in XPS and XAES of solid sulfur compounds. *J. Electron Spectrosc. Relat. Phenom.* **1994**, *68*, 321−328.

(84) Marcus, P.; Protopopoff, E. Potential pH diagrams for sulfur and oxygen adsorbed on nickel in water at 25 and 300° C. *J. Electrochem. Soc.* **1993**, *140*, 1571−1575.

(85) Jiang, N.; Bogoev, L.; Popova, M.; Gul, S.; Yano, J.; Sun, Y. Electrodeposited nickel-sulfide films as competent hydrogen evolution catalysts in neutral water. *J. Mater. Chem. A* **2014**, *2*, 19407−19414.

(86) Jiang, N.; Tang, Q.; Sheng, M.; You, B.; Jiang, D.-e.; Sun, Y. Nickel sulfides for electrocatalytic hydrogen evolution under alkaline conditions: a case study of crystalline NiS, NiS_2, and Ni_3S_2 nanoparticles. *Catal. Sci. Technol.* **2016**, *6*, 1077−1084.

(87) Suzuki, T.; Uchinokura, K.; Sekine, T.; Matsuura, E. Raman scattering of NiS_2. *Solid State Commun.* **1977**, *23*, 847−852.

(88) Guillaume, F.; Huang, S.; Harris, K. D.; Couzi, M.; Talaga, D. Optical phonons in millerite (NiS) from single-crystal polarized Raman spectroscopy. *J. Raman Spectrosc.* **2008**, *39*, 1419−1422.

(89) Cheng, Z.; Abernathy, H.; Liu, M. Raman spectroscopy of nickel sulfide Ni_3S_2. *J. Phys. Chem. C* **2007**, *111*, 17997−18000.

(90) Biesinger, M. C.; Payne, B. P.; Lau, L. W. M.; Gerson, A.; Smart, R. S. C. X-ray photoelectron spectroscopic chemical state

quantification of mixed nickel metal, oxide and hydroxide systems. *Surf. Interface Anal.* **2009**, *41*, 324−332.

(91) Fujimoto, T.; Ogawa, S.; Yoshida, T.; Uchiyama, N.; Yagi, S. Hydrogen storage property of Ni nanoparticles fabricated by the gas evaporation method. *Surf. Interface Anal.* **2014**, *46*, 1121−1124.

(92) Zhao, Y.; E, Y.; Fan, L.; Qiu, Y.; Yang, S. A new route for the electrodeposition of platinum−nickel alloy nanoparticles on multi-walled carbon nanotubes. *Electrochim. Acta* **2007**, *52*, 5873−5878.

(93) Prieto, P.; Nistor, V.; Nouneh, K.; Oyama, M.; Abd-Lefdil, M.; Díaz, R. XPS study of silver, nickel and bimetallic silver−nickel nanoparticles prepared by seed-mediated growth. *Appl. Surf. Sci.* **2012**, *258*, 8807−8813.

(94) Legrand, J.; Gota, S.; Guittet, M. J.; Petit, C. Synthesis and XPS characterization of nickel boride nanoparticles. *Langmuir* **2002**, *18*, 4131−4137.

(95) Konopka, S.; McDuffie, B. Diffusion coefficients of ferri-and ferrocyanide ions in aqueous media, using twin-electrode thin-layer electrochemistry. *Anal. Chem.* **1970**, *42*, 1741−1746.

(96) Spek, A. L. Structure validation in chemical crystallography. *Acta Crystallogr., Sect. D: Biol. Crystallogr.* **2009**, *65*, 148−155.

(97) *CrysAlis PRO (CCD and RED)*; Agilent Technologies, 2013.

(98) Dennington, R.; Keith, T.; Millam, J. *GaussView*; Gaussian Inc., 2009.

(99) Sheldrick, G. A Short History of SHELX. *Acta Crystallogr., Sect. A: Found. Crystallogr.* **2008**, *64*, 112−122.

DOI: 10.1021/acs.inorgchem.9b01209
Inorg. Chem. 2019, 58, 12025−12039